Microwave Remote Sensing from Space

KEITH R. CARVER, SENIOR MEMBER, IEEE, CHARLES ELACHI, SENIOR MEMBER, IEEE, AND FAWWAZ T. ULABY, FELLOW, IEEE

Invited Paper

Spaceborne microwave remote sensors provide perspectives of the earth surface and atmosphere which are of unique value in scientific studies of geomorphology, oceanic waves and topography, atmospheric water vapor and temperatures, vegetation classification and stress, ice types and dynamics, and hydrological characteristics. Microwave radars and radiometers offer enhanced sensitivities to the geometrical characteristics of the earth's surface and its cover, to water in all its forms—soil and vegetation moisture, ice, wetlands, oceans, and atmospheric water vapor, and can provide high-resolution imagery of the earth's surface independent of cloud cover or sun angle.

A brief review of the historical development and principles of active and passive microwave remote sensing is presented, with emphasis on the unique characteristics of the information obtainable in the microwave spectrum and the value of this information to global geoscientific studies. Various spaceborne microwave remote sensors are described, with applications to geology, planetology, oceanography, glaciology, land biology, meteorology, and hydrology. A discussion of future microwave remote sensor technological developments and challenges is presented, along with a summary of future missions being planned by several countries.

I. INTRODUCTION

On October 5, 1984, the Space Shuttle *Challenger* carried into space a 1.275-GHz synthetic-aperture radar instrument called the Shuttle Imaging Radar-B (SIR-B). During the 10-day *Challenger* mission, SIR-B acquired high-resolution radar images of the earth's surface, some of which were of selected sites using a variety of illumination angles. This allowed *stereo imagining of the earth's surface*, and the interpretation of morphological features of these sites using three-dimensional viewing and generation of contour maps. Three years earlier, the Space Shuttle *Columbia* carried an earth observations payload including SIR-A, similar to SIR-B except with a fixed illumination angle of 47°. One of the SIR-A image strips was across a hyperarid zone of southern Egypt and northern Sudan. These startling radar images revealed extensive dry river beds beneath the Sahara and subsurface terrain features previously unknown [1]. Subsequent field work confirmed that the radar was *penetrating through* a several-foot thick surficial layer of *very dry aeolian sand* to reveal features of a hidden quaternary alluvial basin.

In 1978, NASA launched Seasat, a polar-orbiting earth observations satellite which carried not only a SAR but a 14-GHz radar scatterometer and other sensors as well. The data obtained using the Seasat X-shaped scatterometer illumination pattern showed that this type of spaceborne microwave remote sensor had the potential for *accurately measuring the magnitude and direction of oceanic winds*. The sensitivity of this 2-cm wavelength scatterometer to oceanic winds is due to the Bragg backscattering of microwaves of centimeter-length ocean waves, i.e., strong reinforcement of backscatter from those ocean surface waves that travel parallel to the radar beam and are twice as long as the horizontal projection of the radar wavelength [2]. The ability to routinely measure oceanic winds at global scales is crucially important to climatological studies as well as the timely prediction of ocean storms and to other problems faced by the physical oceanographer.

One of the Seasat SAR images acquired on August 20, 1978 was of a farmland region of Iowa where a summer squall line had just dumped nearly an inch of rain on a sharply etched region near Cedar Rapids. This spaceborne microwave image demonstrated the *strong sensitivity of microwaves to soil moisture*, confirming earlier ground and aircraft passive and active measurements.

In December of 1972, the Nimbus-5 meteorological research satellite was launched for the purpose of developing measurement techniques for atmospheric processes important in meteorology and general circulation. One of the primary instruments was the Nimbus-5 Microwave Spectrometer (NEMS), a five-frequency passive radiometer operating at two atmospheric water vapor and three oxygen resonant frequencies (see Table 1). This instrument was the first spaceborne microwave temperature sounder, and established that *atmospheric temperature profiles could be measured from space* with an rms accuracy of about 2°C. The physical basis for this measurement lies in the fact that

Manuscript received December 19, 1984; revised January 30, 1985.

K. R. Carver is with the Department of Electrical and Computer Engineering, University of Massachusetts, Amherst, MA 01003, USA.

C. Elachi is with the Jet Propulsion Laboratory, Pasadena, CA 91109, USA.

F. Ulaby is with the Department of Electrical Engineering and Computer Science, University of Michigan, Ann Arbor, MI 48106, USA.

0219/85/0600-0970$01.00

Table 1 Spaceborne Microwave Remote Sensing Missions

Date	Mission	Microwave Sensors	Wavelengths(s)	Purpose
1962	Mariner 2	radiometers	1.9, 1.35 cm	Venus surface temperature
1968	Cosmos 243	radiometers	8.6, 3.4, 1.35, 0.81 cm	atmos. water vapor, ice cover, sea temperature
1972	Nimbus-5	ESMR radiometer	1.55 cm	atmos, rain rate, sea ice
		NEMS radiometers	1.35, 0.96, 0.56, 0.55, 0.51 cm	atmos. temp, water vapor and liquid vapor content
1973	Skylab EREP	S-193 (radiom/ scatt/altimeter)	2.15 cm	simultaneous radar/radiom. measurements of earth surf.
		S-194 radiometer	21.4 cm	soil moisture studies
1975	Nimbus-6	ESMR	0.81 cm	atmos. vapor, sea surface
		SCAMS radiometers	1.35, 0.95, 0.58, 0.56, 0.54 cm	atmos. temp, water vapor and liquid vapor content
1978	Seasat	SAR(radar)	23 cm	sea, land surface imagery
		scatterometer (radar)	2.15 cm	sea surface winds
		altimeter	2.22 cm	sea surface topography
		radiometer (SMMR)	4.54, 2.8, 1.66, 1.42, 0.81 cm	sea surface temperature, wind speed, atmos water vapor
1978	Nimbus-7	SMMR	4.54–0.81 cm	same as Seasat SMMR
1981	Shuttle STS-2	SIR-A (radar)	23 cm	geological mapping
1984	Shuttle STS-17	SIR-B (radar)	23 cm	land, ocean surface studies

atmospheric emission at frequencies around the oxygen resonance complex (centered near 60 GHz) is proportional to atmospheric temperature at altitude levels defined by temperature weighting functions [3].

These examples illustrate but a few of the markedly different ways in which the earth is perceived from space in the microwave spectrum and the type of geoscientific information which is generally not obtainable in other parts of the electromagnetic spectrum. If an astronaut circling the earth were not *homo sapiens*, but instead was some alien creature with the capability of "seeing" with high resolution in the lower part of the microwave spectrum, the view would no longer be one of white clouds, blue oceans, and green vegetation whose appearances depend on the local weather and the sun angle. Instead, the surface would always be seen free of cloud cover and independent of sun angle. There would be a greatly enhanced sensitivity to the geometrical features of the earth's surface and to the geometrical structure of its vegetation cover. The presence of water in all its forms—soil moisture, wetlands, rivers, lakes, fresh and sea ice, etc.—would be revealed in a greatly expanded dynamic range. There would be penetration up to several meters of smooth hyperarid desert areas, perhaps revealing additional subsurface details. If the creature next tuned his gaze to the higher frequency regions of the microwave spectrum, the presence of water vapor, oxygen, and other components of the atmosphere would become much more clear and the meteorological processes would dominate.

Our knowledge of the geoscientific processes of the earth has as its principal antecedent the intuition and learning remotely derived from and measurements made in the optical spectrum. It has been only in the past two decades that we have really begun to "see" a synoptic view of the earth in other portions of the electromagnetic spectrum, and to appreciate the potential of the microwave view in relation to visible and infrared.

The purpose of this paper is to review the current status of spaceborne microwave remote sensing of the earth, and to offer a perspective on future microwave remote sensing scientific applications and missions. The paper begins with a brief review of the physical principles underlying the science of microwave remote sensing, discusses both passive and active microwave remote sensing instruments, points out the potential value of these sensors to various geoscientific disciplines, summarizes recent technological developments, and outlines several future missions currently being planned.

II. Historical Review

The development of both radars and radiometers was begun for purposes other than remote sensing. A variety of radars, including imaging radars, was developed during WWII for military fire control and aircraft tracking. Simple radiometers, consisting of an antenna, low-noise receiver, and strip-chart recorders, were originally developed in the 1930s for use in radio astronomy by such pioneers as Karl Jansky and Grote Reber. Target-oriented military radars were plagued by unwanted clutter from the earth, and the statistical characterization of clutter was a major engineering problem of the 1950s. The first systematic studies of the radar cross section per unit area for land clutter was made in the late 1950s by a group of scientists at Ohio State University [4], who measured the scattering coefficients of various crops, asphalt, concrete, etc. This group also studied the relationship of the passive emissivity of distributed targets to their active scattering coefficients [5].

However, microwave remote sensing for geoscientific studies of the earth did not begin until the mid-1960s when side-looking airborne radars (SLARs) such as the 35-GHz AN/APQ-97, developed by Westinghouse for military reconnaissance, were used by earth scientists for geologic studies. In 1967, the first major airborne radar mapping survey was made of the Oriente Province of Panama [6], which is almost always cloud-covered. The AN/APQ-97 radar was used for both geological and agricultural studies [7].

Spaceborne radar remote sensing utilizes three types of radar: synthetic-aperture radars (SAR), scatterometers, and altimeters. NASA's Skylab and Seasat missions were the first

to include several types of radar remote sensors as well as radiometers for earth observations, as indicated in Table 1. The manned Skylab missions operated by NASA between May 1973 and February 1974 carried a combination microwave radiometer/scatterometer and altimeter instrument, designated S-193, operating at 13.9 GHz [8], as well as an *L*-band radiometer (S-194). The unmanned Seasat satellite was launched into near polar orbit in June 1978 and carried several microwave instruments dedicated to oceanic observations: 1) an *L*-band SAR with a 20° incidence angle, 100-km swath, and 25-m spatial resolution [9], 2) the Seasat-A Satellite Scatterometer (SASS), a 13.9-GHz radar with an X-shaped illumination pattern for oceanic wind-wave measurements, 3) a 13.5-GHz altimeter which achieved an altitude measurement precision of better than 10 cm and significant wave height accuracy of ±50 cm; Seasat also included both microwave and visible/IR radiometers. The SASS instrument on Seasat was included because of data from earlier airborne scatterometers flown by NRL and NASA Johnson Space Center that showed that the backscattering coefficient from the sea is proportional to a power of the wind speed [10]; indeed, during the three months that Seasat was operational, a large library of data was recorded which confirmed the sensitivity of centimeter-wavelength radar backscatter to wind-driven oceanic capillary waves.

Microwave radiometry from space began with studies of planetary emission. A microwave radiometer with 15.8- and 22.2-GHz channels carried by Mariner 2 on its December 1962 flyby of Venus made three scans of the planetary disc, confirming the high temperature of the Venusian surface and showing that its planetary emission was characterized by limb-darkening [11]. However, the first microwave radiometric observations of the earth from space were not made until 1968, when the Soviet satellite Cosmos 243 was launched. A nonscanning, nadir-viewing 4-channel radiometer was used to estimate atmospheric water vapor, liquid water, ice cover, and sea temperature [12]. This experiment was followed by a number of Soviet and US earth-viewing radiometer missions, carrying instruments of progressively increased sophistication. The Nimbus-5 spacecraft was launched in 1972, and carried two primary microwave radiometers: 1) the Electronically Scanned Microwave Radiometer (ESMR), a 19.3-GHz imaging radiometer for measuring atmospheric rain rate and sea-surface ice, and 2) the Nimbus-E (5) Microwave Spectrometer (NEMS), a five-frequency nadir-viewing radiometer designed to measure atmospheric temperature profiles, water vapor content, and liquid vapor content. Nimbus-6, launched in June 1975, included the Scanning Microwave Spectrometer (SCAMS) radiometer. SCAMS, like NEMS, was used to determine atmospheric temperature profiles and atmospheric liquid water and water vapor over ocean surfaces [13]. The 5-channel Scanning Multichannel Microwave Radiometer (SMMR) instrument, included on both Nimbus-7 and Seasat, provided additional capabilities over NEMS including the measurement of sea-surface temperature and wind speed.

The Seasat SAR was the first to provide high-resolution imagery of the earth's surface from satellite altitudes. It was operated at a single wavelength (23 cm), with HH polarization (horizontal transmit, horizontal receive) and at a fixed incidence angle of 20° (from nadir). The next spaceborne SAR to be launched was the Shuttle Imagining Radar-A (SIR-A), launched on November 12, 1981 on the Space Shuttle *Columbia* (STS-2) in a 28.5° inclination orbit. SIR-A, like the Seasat SAR, was an *L*-band HH-polarized instrument, but the angle of incidence was fixed at 47°. SIR-B, launched on the Space Shuttle *Challenger* (STS-17) in October 1984, was also an *L*-band HH-polarized SAR, but could mechanically tilt the antenna to achieve variable incidence angles. Whereas the SIR-A data were optically recorded and correlated, SIR-B images were digitally recorded and processed.

III. Review of Microwave Remote Sensing Principles

A. Microwave Spectrum

The microwave spectrum which has been used for remote sensing extends from about 500 MHz to 100 GHz. Table 2 shows some commonly used frequencies or wavelengths, and letter band designations for both active and

Table 2 Commonly Used Radar and Radiometer Bands

Frequency	Wavelength	Band	Mode	Sensors
400 MHz	75 cm	*P*	passive	aircraft radiometer
1275 MHz	23.5	*L*	active	Seasat SAR, SIR-A/B
1400 MHz	21.4	*L*	passive	Skylab S-194 Radiometer
3500 MHz	8.6	*S*	passive	Cosmos 243 Radiometer
5200 MHz	5.7	*C*	active	aircraft scatterometer
6600 MHz	4.5	*C*	passive	Nimbus-7, Seasat SMMR
8800 MHz	3.4	*X*	passive	Cosmos 243 radiometer
9600 MHz	3.1	*X*	active	aircraft scatterometer
10.7 GHz	2.8	*X*	passive	Nimbus-7, Seasat SMMR
13.5 GHz	2.22	*Ku*	active	Seasat altimeter
13.9 GHz	2.15	*Ku*	active	Seasat SASS, Skylab S-193
18.0 GHz	1.66	*K*	passive	Nimbus-7, Seasat SMMR
19.3 GHz	1.55	*K*	passive	Nimbus-5—ESMR
21.0 GHz	1.43	*K*	passive	Nimbus-7, Seasat SMMR
22.2 GHz	1.35	*K*	passive	Nimbus-5—NEMS, Cosmos 243
31.4 GHz	9.55 mm	*Ka*	passive	Nimbus-5—NEMS
35 GHz	8.57	*Ka*	active	AN/APQ-97 aircraft SLAR
37.5 GHz	8.00	*Ka*	passive	Cosmos 243 radiometer
53.6 GHz	5.60	*Q*	passive	Nimbus-5—NEMS
96 GHz	3.13	*W*	passive	radiometer

passive microwave remote sensors. Frequencies which have been used for spaceborne remote sensing range from *L*-band (1.3 GHz) through *Q*-band (58 GHz).

1) Atmospheric Transmissivity: At frequencies above about 20 GHz, microwave signals passing through the earth's atmosphere are significantly attenuated due to absorption by water and oxygen molecules, as shown in Fig. 1. The

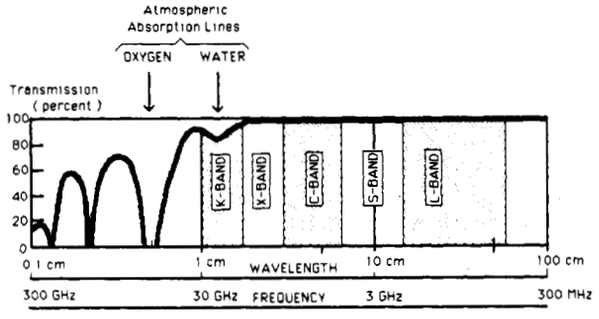

Fig. 1. Atmospheric transmission coefficient (percent) versus frequency at zenith with several microwave bands indicated.

exact shape of the attenuation profile depends on the distribution of atmospheric water vapor [14]. The attenuation peak near 22 GHz is the pressure-broadened absorption line due to atmospheric water vapor and that near 60 GHz is a broadened complex of O_2 absorption lines.

The frequency range 1–20 GHz has been used primarily for passive and active remote sensing of the earth's land and ocean surface, due in part to the low attenuation of the atmosphere and in part to naturally enhanced sensitivities in this frequency range to such surface features as soil moisture and ocean capillary waves. Frequencies above 20 GHz have been used primarily for spaceborne sensing of atmospheric water vapor, oxygen, and temperature, although as pointed out earlier the diffraction-limited AN/APQ-97 SLAR operating in the 35-GHz atmospheric window was used from aircraft altitudes for some of the first geological mapping applications.

2) Comparison to Optical Remote Sensing: Information gained through microwave remote sensing techniques is generally quite different from but complementary to that obtained from optical (visible/IR) methods. As discussed below, microwave remote sensors used for surface sensing provide cloud-free data that are especially sensitive to surface geometry and the presence of water. By contrast, optical reflectivities are more sensitive to surface chemistry.

3) Unique Features of Microwave Remote Sensing: Microwave remote sensing provides data with unique sensitivities and other features not found in thermal IR or optical/near IR data.

a) Sensitivity to surface geometry: Backscattered radar waves are very sensitive to the geometrical features of the earth's surface as well as the geometrical structure of cultural and natural cover. Radar backscattering from terrain is particularly responsive to surface slope at both small incidence angles (less than about 30°) and large angles (larger than about 55°). As pointed out previously, centimeter-wavelength radar backscattering from the sea shows a strong dependence on the Bragg scattering from capillary and short gravity waves; again, this is basically a response to the geometry of these waves. Finally, recent research has shown that the radar response to vegetation such as trees, cultivated crops, etc., is strongly dependent on their geometrical structure (size and shape of stalks, trunks, branches, leaves) as well as their moisture content.

b) Sensitivity to water: Water is a highly polarized molecule and has a high dielectric constant (about 80) in the lower regions of the microwave spectrum. This means that the reflectivity of water is very high and that its emissivity is intrinsically low. To a radar, the presence of increased water either in soils with a rough surface or vegetation shows up as increased backscatter; to a radiometer, increased water content is seen as a decrease in brightness temperature. The dielectric constant of ice and hence its reflectivity/emissivity is highly sensitive to the degree of salinity. This means that microwave radars and radiometers can be used not only for ice mapping but also for distinguishing first-year from multi-year ice in polar regions.

As the frequency is increased to about 22 GHz and above, a different expression of water is seen in the form of the rotational absorption and emission of microwaves by atmospheric water vapor and oxygen. Because atmospheric water vapor is especially dependent on temperature, it then becomes possible to remotely sense atmospheric temperature profiles as was done with the Nimbus-5 NEMS instrument.

c) Independence of cloud cover or sun angle: Imaging radars such as the Seasat SAR provide the capability to obtain high-resolution surface images independent of cloud cover and at any time of day or night. This is essential for some applications such as oceanographic monitoring, since the observations and forecasting of oceanic winds normally takes place in or near cloud-covered storm cells. It is also important for mapping of perennially cloud-covered regions such as the Brazilian jungle.

Optical images of the earth such as acquired by Landsat are normally recorded with a fixed sun angle for purposes of providing constant illumination. This means that sun-synchronous orbits are required. Since imaging radars provide their own illumination, there is no dependence on sun angle and a greater choice of orbital altitude is afforded.

B. Principles of Passive Microwave Remote Sensing

This section presents a very brief review of some of the basic terminology used in passive microwave radiometry. For further details, the reader may consult other papers and books devoted to the subject. A good point of departure is the comprehensive review article on passive microwave remote sensing from space recently published by Njoku [3]. The reader is also directed to Chapter 11 of the *Manual of Remote Sensing*, Volume 1 [15] and to the comprehensive discussions given in Volumes 1, 2, and 3 of the book *Microwave Remote Sensing* [16]–[18].

1) Thermal Radiation, Blackbodies, Emissivity, and Brightness Temperature: All objects not at absolute zero temperature emit weak electromagnetic energy as a result of thermally induced random motions of electrons and protons. This emission is in the form of noisy electromagnetic waves, with all frequency components. Moreover, the directions of these charged particles is basically random with the

result that the polarization of this thermally induced electromagnetic radiation is essentially random. For objects with temperatures near ambient, i.e., about 300 K, the thermal radiation is maximum in the "thermal infrared" portion of the spectrum, i.e., at wavelengths near 10 μm. Thermally emitted noise waves are about six orders of magnitude weaker in the microwave spectrum, yet can be easily detected by a microwave radiometer.

A microwave radiometer consists essentially of an antenna, a very sensitive receiver, and a recorder, as shown in Fig. 2(a). It is used to measure the thermally emitted noise waves from the earth's surface or atmosphere. If the antenna is modeled as a noise-generating resistor at temperature T, the available noise power from the antenna is given by $P = kT\Delta f$, where $k = 1.23 \times 10^{-23}$ J · K^{-1} (Boltzmann's constant) and Δf is the bandwidth of the receiver. In fact, the output of a calibrated microwave radiometer is expressed as a so-called "antenna temperature" T_A, which is proportional to the total noise power resulting from the thermal radiation incident on the antenna. Referring to Fig. 2(b), the antenna temperature is given by

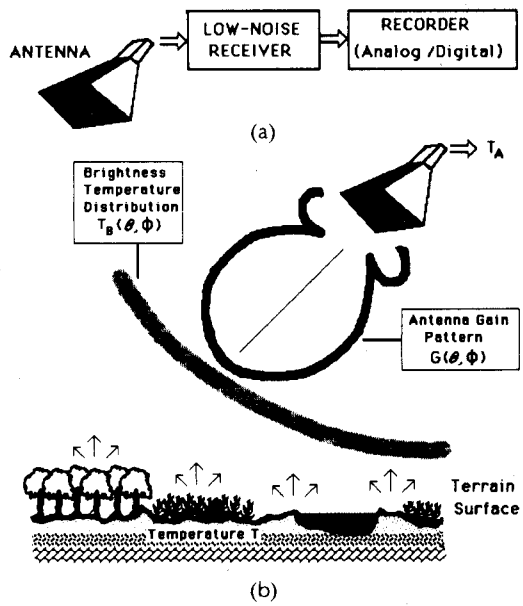

Fig. 2. (a) Simple microwave radiometer showing antenna, receiver, and recording device. (b) A brightness temperature distribution $T_B(\theta,\phi)$ incident on an antenna with a gain pattern $G(\theta,\phi)$.

$$T_A = \frac{1}{4\pi}\iint_{4\pi} T_B(\theta,\phi)\, G(\theta,\phi)\, d\Omega \qquad (1)$$

where $G(\theta,\phi)$ is the antenna gain pattern, and $T_B(\theta,\phi)$ is the *brightness temperature distribution* incident on the antenna. The antenna temperature is essentially the sum of the antenna pattern-weighted contributions from the brightness temperature distribution over a range of angles.

The brightness temperature T_B is a term used to indicate the intensity of thermal radiation upwelling from the earth's surface or atmosphere. If a thermally radiating object were a perfect radiator and absorber of electromagnetic energy, i.e., a *blackbody*, the brightness temperature would be equal to the absolute temperature of the object. If the antenna were surrounded by a perfect blackbody, its antenna temperature would be equal to the physical temperature of the object. Perfect blackbodies do not exist in nature, and the brightness temperature of radiating objects such as terrain, sea, or the atmosphere is always less than the physical temperature. The *emissivity* of an object is a dimensionless quantity which indicates how good a blackbody it is. The emissivity of a thermally radiating object is given by

$$e(\theta,\phi) = \frac{T_B(\theta,\phi)}{T} \qquad (2)$$

where $T_B(\theta,\phi)$ is its brightness temperature distribution and T is its absolute physical temperature. The emissivity is a dimensionless quantity which ranges from 0 to 1. The emissivity of a perfect blockbody is unity and for a perfect reflector it is zero. The emissivity depends on the material composition and geometrical shape of the radiating object, and is also dependent on the frequency of observation and polarization of the microwave radiometer. For a much more complete description of thermal radiation, brightness temperatures, and emissivity the reader is referred to [15]–[18].

The brightness temperature distribution incident on a spaceborne microwave radiometer directed toward the earth is generally due both to radiation from the earth's surface as well as its atmosphere. The brightness temperature distribution is composed of radiation self-emitted from terrain or sea, upward emission from the atmosphere, and downward atmospheric emission that is rescattered by the surface back toward the antenna. In addition, the surface emission and rescattered components are attenuated by the atmosphere as they propagate back toward the antenna.

At microwave frequencies below about 10 GHz, the atmospheric absorption and emission is small and can be essentially neglected. At these frequencies, the brightness temperature distribution is given simply by

$$T_B = e_i(\theta,\phi)\, T \qquad (3)$$

where e is the emissivity of the earth's surface (terrain or sea), i denotes the polarization (horizontal or vertical) of the observing radiometer, and T is the physical temperature of the surface (see Fig. 3). At X-band and higher frequen-

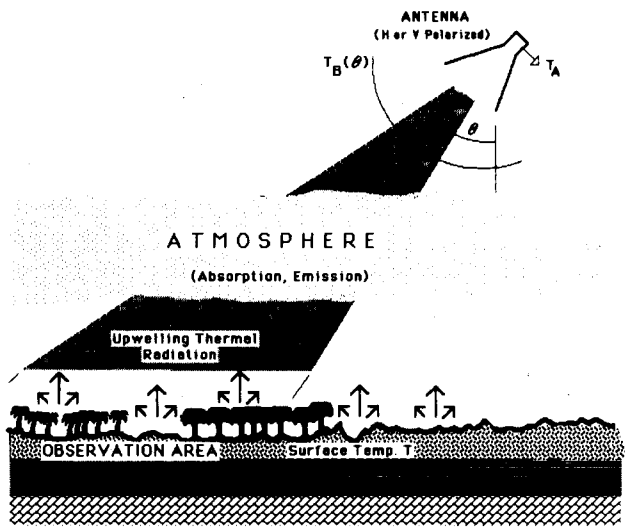

Fig. 3. Illustrating thermal emission process from earth, and radiative transfer of thermal noise energy to a spaceborne radiometer.

cies, the atmospheric contributions are significant and must be included. For a much more complete discussion of microwave interaction with atmospheric constituents, the reader is referred to an excellent paper by Staelin [19] or to [16, ch. 5].

A short discussion of the brightness temperature behavior of the sea surface and various terrain surfaces is next presented, along with references for further reading.

a) Brightness temperature of the sea: The brightness temperature of the sea depends not only on its physical temperature, but also on its roughness (in relation to the wavelength) and salinity as well as the observing angle from nadir, observing frequency, and polarization. The sea surface roughness depends in turn on the wind speed. For a calm (specular) sea at a temperature of 20°C and a salinity of 36 parts per thousand, the nadir brightness temperature varies from about 90 K at 1.4 GHz to 110 K at 10 GHz to 130 K at 37 GHz. As the angle from nadir increases, the horizontally polarized component of the brightness temperature decreases and the vertically polarized component increases. As the salinity decreases from 36 ‰ to 0‰ (fresh water), the nadir brightness temperature increases by a few degrees [20], [61]. As the wavelength becomes shorter, sensitivity to surface roughness and wind increases. For example, at about 19 GHz and a 55° angle from nadir, the horizontally polarized component of the brightness temperature increases approximately linearly with increasing wind speed, from about 82 K at zero wind speed to 96 K at a 14-m/s wind speed [21], when neither foam nor whitecaps are present. For more information on passive microwave remote sensing of the sea, the reader is referred to [22]–[24].

b) Brightness temperature of sea ice: When sea water is covered by an ice sheet, the combined emissivity is different from either that of ice or sea water. Sea ice is basically a mixture of ice, salt, bubbles, and pockets of brine, and the sea ice–air boundary may be smooth or rough. At angles close to nadir, surface emission processes dominate while at larger angles, both surface and volume scattering processes are important. The processes of emission and scattering are complicated and depend strongly on wavelength and polarization [25], [26].

The differing emissivities of open sea water, first-year sea ice, and multiyear sea ice form the basis for passive microwave remote sensing on a global scale of the polar ice regions [28]–[31]. For example, satellite observations during the winter of 1973 by the Nimbus-5 ESMR (19.35-GHz) mapping instrument demonstrated an ability to distinguish multi-year ice covering the main part of the Arctic Ocean (brightness temperatures ranging from 209 to 223 K) from first-year ice with higher brightness temperatures on the southern portions of the ocean. By the following summer, most of the marginal zone sea ice had melted and the ESMR images show a marked difference. The images collected by ESMR provide a dramatic demonstration of the potential of passive microwave remote sensing techniques to provide new and valuable information on sea ice morphology and dynamics [27].

c) Brightness temperature of terrain: The emissivity of bare soil depends strongly on surface roughness and soil moisture, as well as the observation parameters of wavelength, incidence angle, and polarization. At the lower microwave frequencies (e.g., 1.4 GHz) soil moisture variations have a pronounced effect on the brightness temperature. The strong dependence of the soil emissivity on its moisture content is due to the high dielectric constant of water (approximately 80) in contrast to that of dry soil (about 3–4). As the moisture in the soil increases, the dielectric constant of the wet soil can reach 20 or more, resulting in an emissivity change at 1.4 GHz from about 0.95 for dry soil (volume moisture content less than 0.1 g/cm^3) to 0.6 for wet soils (greater than 0.3 g/cm^3) [32].

Despite a strong sensitivity of the emissivity on soil moisture, microwave remote sensing of soil moisture from space is complicated by the confusion factors of surface roughness and vegetation cover which also affect the brightness temperature. For example, a nadir-viewing *L*-band radiometer viewing a bare field with a uniform moisture level (0.34 g/cm^3) would see a typical emissivity of 0.55 with a 4-cm rms surface roughness and an emissivity of 0.70 when the surface roughness was reduced to 0.8 cm [33]. The emissivity of vegetated terrain depends on three factors: 1) emission from the underlying soil as attenuated by the vegetation layer, 2) upwelling emission from the vegetation layer itself, and 3) vegetation layer emission reflected by the soil surface and attenuated by the vegetation layer. In effect, the presence of vegetation reduces the radiometric sensitivity to soil moisture over that for bare soils alone [18]. At *L*-band, for example, the reduction in sensitivity to soil moisture can range from 15 to 60 percent for crops and grasses and approximates 80 percent for forest trees [34], [35].

d) Brightness temperature of snow: The emissivity of snow-covered soil in general depends on the dielectric constant of the underlying frozen soil (approximately 3) and the thickness, water equivalent, and liquid water distribution in the snow layer. The dependence is more pronounced at frequencies at or above *X*-band, where the snow layer is electrically thicker. For a layer of dry snow, as the snow water equivalent (i.e., the total snow mass of water in a vertical column) increases, the brightness temperature decreases [36]. However, for wet snow, even a small increase in the amount of liquid water (snow wetness) causes the brightness temperature to rise [37], [38], due to volume scattering.

C. Principles of Radar Remote Sensing

Both imaging and nonimaging radar systems are used in remote sensing. Nonimaging radars include scatterometers, which measure the scattering properties of distributed targets, and altimeters, which are nadir-looking short-pulse radars used to measure the height of the radar's platform above the ground surface. A scatterometer usually measures the range (distance) to the scattering target R in order to calculate the backscattering coefficient σ° from the received power P_r. (The backscattering coefficient σ° of an area-extensive target is defined as the radar cross section of the target per unit area.) An altimeter is similar to a scatterometer except that its primary function is to measure R, rather than σ°, as accurately as possible.

As a precursor to describing the operation of imaging radar systems, let us consider the scatterometer system depicted in Fig. 4. A transmitter unit and a receiver unit are connected to a common antenna through a circulator which allows signals to flow in a clockwise direction only. The main beam of the antenna illuminates an ellipse on the

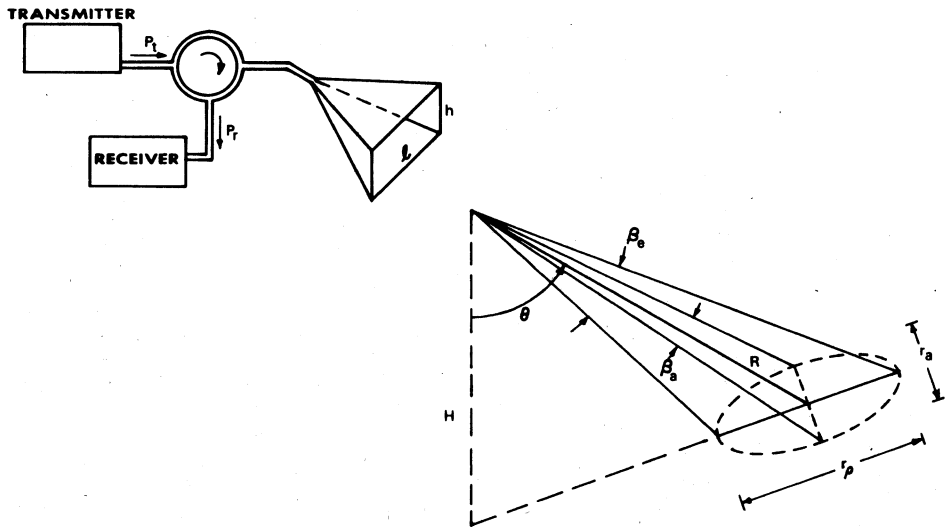

Fig. 4. Simple scatterometer system illuminating an elliptical ground area from a height H.

ground defined by axes r_a and r_ρ, where the subscripts a and ρ denote the azimuth and ground-range directions, respectively. The values of r_a and r_ρ may be determined from the antenna beamwidths β_a and β_e and the range R

$$r_a = \beta_a R \tag{4a}$$

$$r_\rho = R\left[\sin\left(\theta + \frac{\beta_e}{2}\right) - \sin\left(\theta - \frac{\beta_e}{2}\right)\right] \tag{4b}$$

where θ is the incidence angle corresponding to the range R. The azimuth beamwidth is given by

$$\beta_a = K\frac{\lambda}{\ell} \tag{5}$$

where K is an antenna illumination factor which varies typically from 0.5 to 2 and ℓ is the antenna length. A similar equation relates β_e to the antenna height dimension h.

In the general case, the transmitted power P_t incident upon the illuminated target is related to the received backscattered power P_r through an integral form of the radar equation. If the beamwidths β_a and β_e are small (each less than a few degrees), the following approximate form of the radar equation may be used [39]:

$$P_r(\theta) = \left[\frac{P_t G^2 \lambda^2}{(4\pi)^3 R^4}\right]\sigma^\circ_{rt}(\theta) \tag{6}$$

where G is the antenna gain, λ is the wavelength, and $\sigma^\circ_{rt}(\theta)$ is the backscattering coefficient of the illuminated area for illumination by a t-polarized wave and reception by an r-polarized antenna. Remote sensing radars usually operate in one or more of the following polarization modes: HH, VV, or cross, where HH denotes that both the transmit and receive antennas are horizontally polarized, VV denotes vertical polarization, and cross (HV or VH) denote that one of them is horizontally polarized and the other is vertically polarized. The backscattering coefficients corresponding to these modes are σ°_{hh}, σ°_{vv}, and σ°_{hv} or σ°_{vh} (the reciprocity theorem states that $\sigma^\circ_{vh} = \sigma^\circ_{hv}$).

The quantities inside the brackets on the right-hand side of (6) are either system or propagation parameters; therefore, they bear no direct relationship to the scattering properties of the illuminated area. In other words, differences in received power for adjacent pixels on a radar image are entirely due to corresponding differences in the magnitudes of their scattering coefficients. If an imaging radar has been calibrated on an absolute scale, it can be made to produce a σ° image. The relationships between $\sigma^\circ_{rt}(\theta)$ and the physical properties of terrestrial surfaces and volumes are discussed below.

1) Imaging Radar Fundamentals: Most imaging radars used in remote sensing are side-looking airborne radars (SLARs). A rectangular antenna is usually employed, with the long side oriented along the direction of motion of the platform, and the antenna aperture positioned such that the antenna beam points to the side of the platform. Since the antenna beamwidth in a given plane is approximately equal to the inverse of the antenna dimension in that plane (measured in wavelength units), as indicated by (5), the SLAR antenna has a fan-shaped beam (Fig. 5) with its

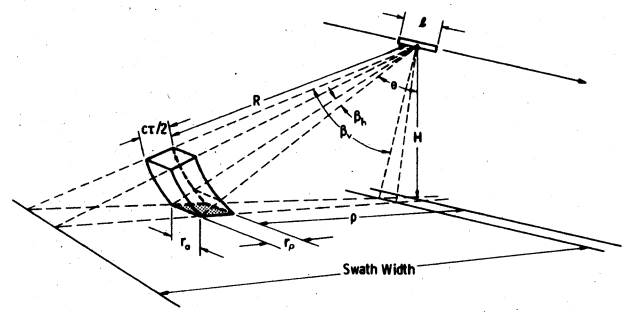

Fig. 5. Real-aperture SLAR geometry and received surface element with area $r_\rho \times r_a$.

narrow side in the along-track or azimuth direction and its wide side in the cross-track or range direction. In the absence of any modulation of the transmitted signal, the ground resolution of the system would simply be the area illuminated by the antenna beam. With an aircraft SLAR, the antenna is mounted on the belly of the aircraft; consequently, its size is limited by the size of the aircraft. From aircraft altitudes, this limitation leads to illuminated areas with range dimensions of the order of kilometers and

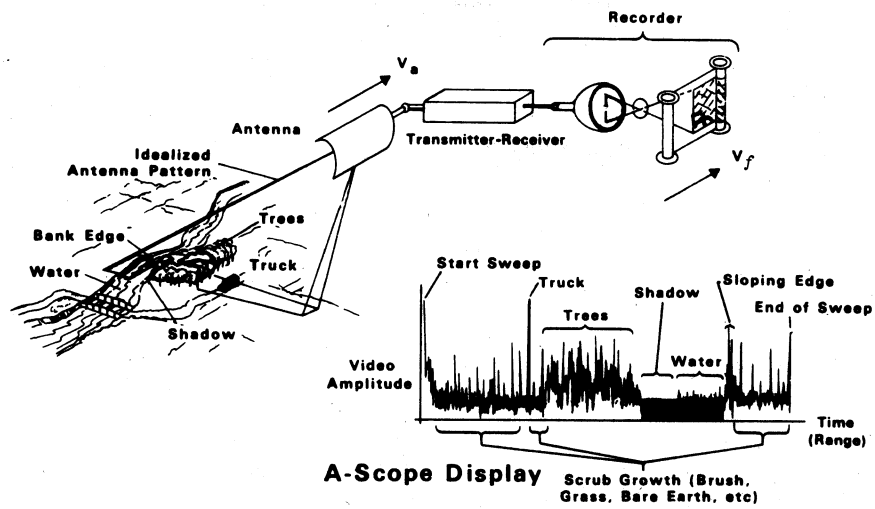

Fig. 6. Real-aperture SLAR technique. The return signal is used to generate an intensity-modulated scan line on a cathode-ray tube display and then transferred to film by a lens. The film is made to move at a speed proportional to that of the aircraft.

azimuth dimensions of the order of tens of meters. Even though satellite platforms can carry antennas that are larger in size than those that can be mounted on the bellies of aircraft, the much larger range between a satellite SLAR antenna and the ground leads to very large illuminated ground areas.

The range resolution problem can be solved easily by means of the transmission of short pulses. For a pulse of width τ, the range resolution r_ρ for incidence at an angle θ is given by

$$r_\rho = \frac{c\tau}{2\sin\theta} \tag{7}$$

where c is the velocity of light.

SLARs that depend upon the antenna beamwidth to attain resolution in the azimuth direction and on the pulsewidth to attain resolution in the range direction are known as real-aperture radars (RARs). The image formation process is illustrated in Fig. 6.

If, in addition to using short pulses for range resolution, a long antenna is generated synthetically in the azimuth direction by recording and processing the backscattered energy from many successive pulses, good resolution can be obtained in the azimuth direction as well, as shown in Fig. 7. This is the basic principle of the SAR whose azimuth resolution is independent of the slant range R and is equal to one half the antenna length

$$r_a = \ell/2. \tag{8}$$

To obtain this resolution, SAR processing must involve the phase history of the return signal over a synthetic aperture of length equal to the azimuth resolution of the real aperture. Additionally, to "focus" the synthetic aperture to the desired slant range, a quadratic phase correction must be applied to the signals received at the different points in the synthetic aperture. SAR systems have superior resolution capabilities over RAR systems, although they are also much more complicated both in terms of their construction and signal processing. For more detailed information on RAR and SAR systems, the reader is referred to [17, chs. 8 and 9].

2) Radar Backscattering and Surface Penetration: The radar cross section σ of a point target such as an aircraft,

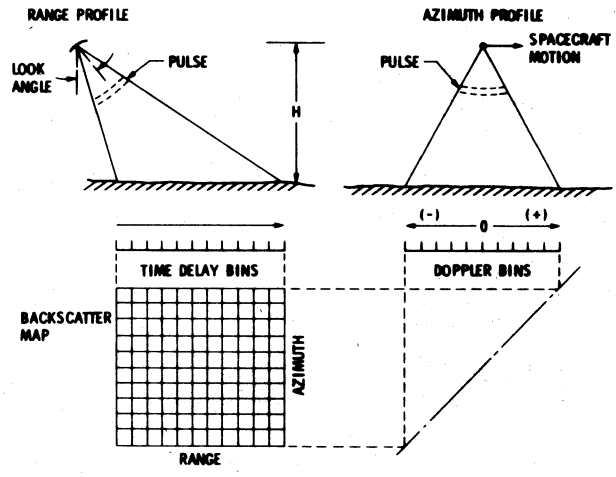

Fig. 7. Synthetic-aperture radar (SAR) technique. The amplitude and phase histories of the return signal are recorded for many pulses covering a synthetic aperture of length equal to the azimuth resolution of the real aperture; these pulses are later processed to attain an azimuth resolution $r_a = \ell/2$, where ℓ is the length of the real aperture.

building, truck, etc., is a measure of its effective area in scattering an incident wave in some given direction, and has units of square meters. The radar cross section is an angularly dependent function whose shape can be thought of as the antenna pattern of a point target for a given illumination angle. When the scattering angle is equal to the illumination angle, the signal is said to be backscattered. This is the situation with most radars.

Radar remote sensing deals principally with area-extensive targets such as terrain or sea surfaces instead of individual point targets. Again, most practical radars such as altimeters, scatterometers, and SARs are used to record the backscattered radar signals. The intensity of the backscattered signals from area-extensive targets is measured in terms of the radar backscattering coefficient σ°, which is defined to be the radar cross section of the distributed target per unit area. The backscattering coefficient σ° is a dimensionless quantity which actually has the units of square meters per square meters.

Referring to Fig. 8, a surface which is rough with respect to a wavelength exhibits diffuse scattering characteristics, i.e., the backscattered signal may be comparable in intensity to the forward scattered signal. A calm water surface scatters most of the incident energy in the forward direction, so that the radar backscattering coefficient is very small. Because of the high dielectric constant of water, there is essentially no radar penetration of water at L-band or higher frequencies, although subsurface features which affect the surface roughness are sometimes evident.

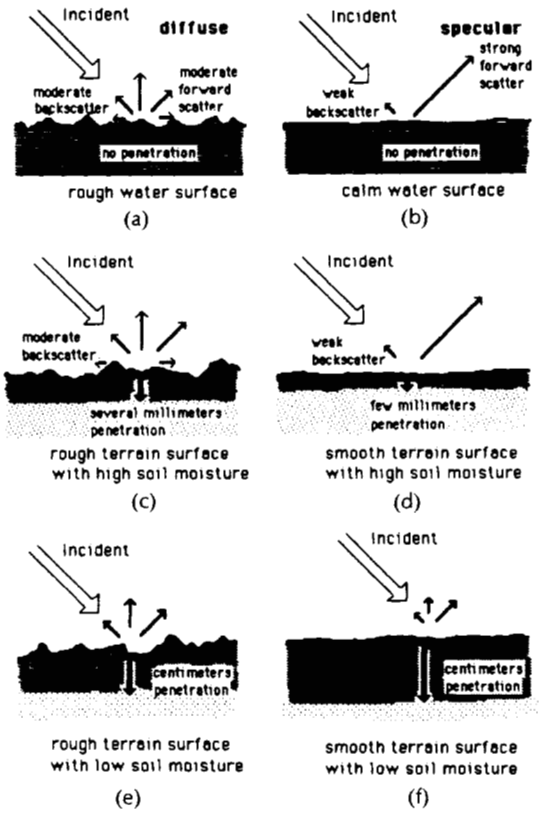

Fig. 8. (a) An incident radar wave on a rough water surface scatters in a diffuse fashion with only weak dependence on scattering angle, and moderate backscatter. (b) When the water surface is calm, the scattering is specular, with most of the energy scattering in the forward and relatively little in the direction back toward the radar. There is virtually no penetration of the water because of its high dielectric constant. (c) An incident wave on rough terrain surface with high soil moisture also scatters diffusely, and a very small penetration of the soil takes place. (d) When the wet soil is relatively flat, there is strong specular scattering away from the radar. (e) and (f) When the soil is dry (e.g., sandy soil in arid regions), there can be penetration ranging from a few centimeters to a few meters, depending on soil aridity.

Most natural terrain materials are partially transparent at microwave frequencies. Again referring to Fig. 8, where a wave is incident upon a terrain surface, part of its power is scattered back into the air and the remainder is transmitted across the boundary into the terrain. The component scattered by the surface is referred to as the surface scattering contribution. If the terrain medium is spatially inhomogeneous (Fig. 8(f)) then volume scattering from the inhomogeneities can take place and the component backscattered across the boundary toward the radar is referred to as the volume scattering contribution. The penetration depth δ_p of a medium is defined as that depth below the surface at which the magnitude of the power of the transmitted wave is equal to 36.8 percent ($1/e$) of the power of the transmitted wave at a point just beneath the surface. In the majority of situations, the vertical extent (in the medium) of the region responsible for the majority of the backscattered energy received by the radar is on the order of one to three times the penetration depth δ_p.

The penetration depth δ_p is determined by both absorption and scattering losses. Absorption losses may be readily computed if the average dielectric constant of the medium is known. Computation of scattering losses is more complicated because it involves the shape, size, and dielectric constant of the scattering elements. An upper estimate of the penetration depth may be obtained by ignoring scattering losses, which often provides a reasonable estimate of δ_p because in the majority of cases absorption losses far exceed scattering losses.

The two most important parameters governing the absorption coefficient of a natural material are the wavelength and the material's liquid water content m_v. This is illustrated by the curves in Fig. 9 which depict the variation of δ_p as a function of m_v for soil and snow at several microwave frequencies. Note that exponential-like decrease of δ_p with m_v and the strong dependence of frequency.

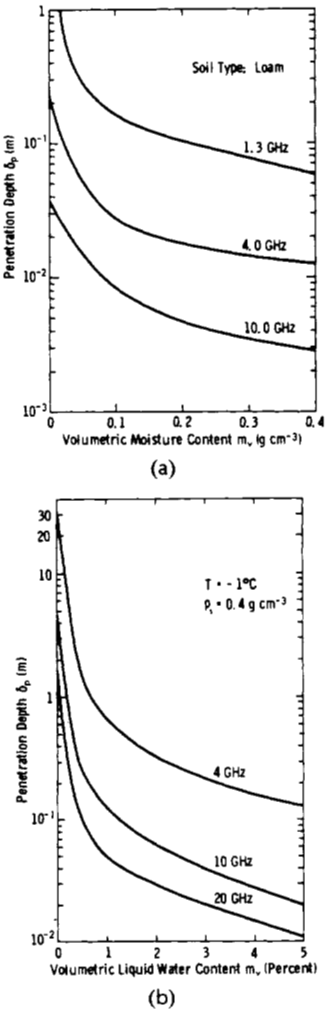

Fig. 9. Penetration depth of (a) loamy soil and (b) snow, both as a function of liquid water content (Ulaby *et al.* [17]).

3) Backscattering Behavior of Natural Targets:

a) Angular variations: The scattering behavior of a distributed target is specified when the backscattering coefficient σ° is known as a function of incidence angle, frequency, and polarization. For a given angle, frequency, and polarization, the backscattering coefficient is governed by the target's dielectric and geometrical properties. Fig. 10 illustrates the dependence of $\sigma^\circ(\theta)$ on incidence angle for slightly rough, moderately rough, and very rough surfaces.

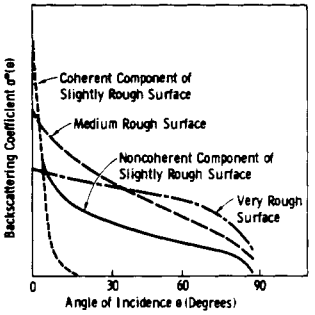

Fig. 10. Angular variation of the backscattering coefficient for different surface roughness conditions.

This dependence is analogous to the gain pattern of a 1-m^2 antenna aperture (actually the terrain surface area) and indicates that σ° is largest at normal incidence. As the incidence angle departs from normal, the backscattered coefficient decreases at a rate which depends on the surface roughness. For diffuse surfaces (rms roughness large with respect to a wavelength), the backscattered signal is not a strong function of incidence angle, while for specular surfaces (electrically flat), the backscattered signal is a very strong function of incidence angle. In practice, σ° is expressed in decibels, i.e., $\sigma^\circ(\text{dB}) = 10 \log \sigma^\circ$. The dependence of σ° on the dielectric constant of the target is illustrated in Fig. 11 which shows curves for relatively dry

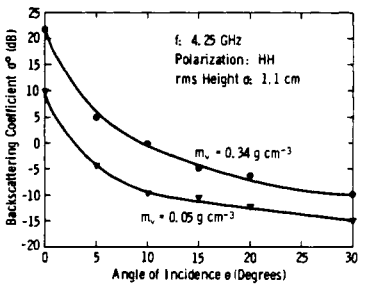

Fig. 11. Comparison of the backscattering coefficient for wet and dry soil.

and wet soil surfaces characterized by volumetric moisture contents of 0.05 and 0.34 g · cm^{-3}, respectively. The corresponding dielectric constants are $\epsilon_r = 3.1 - j0.1$ for the dry soil and $\epsilon_r = 21 - j4.8$ for the wet soil. The difference in level between the two curves is a direct consequence of the difference in dielectric constants of the two soils.

b) Spectral variation: The wavelength of an incident wave plays a major role in radar backscattering from surfaces and volumes. The penetration depth δ_p—which determines the thickness of the surface layer contributing the majority of the backscattered energy—decreases with increasing frequency, and the variation is as f^{-2} to f^{-3} [39]. At a given wavelength λ, the roughness of a surface is characterized in terms of the spatial-frequency spectrum of $z(x, y)/\lambda$ where $z(x, y)$ is the surface-height variation. Thus the scale of surface roughness increases with decreasing wavelength (increasing frequency), leading to a weaker dependence of σ° on the incidence angle (see Fig. 10).

A medium is considered electromagnetically inhomogeneous it if contains inclusions whose a) dielectric properties are different from those of the host (background) material and b) sizes are comparable to or larger than the wavelength in the medium λ_m (which is equal to the free-space wavelength λ divided by the average index of refraction of the medium η_m). Thus as in the case of surface scattering, the degree of inhomogeneity is measured relative to the wavelength λ. This leads to the greater importance of diffuse scattering within the volume with increasing frequency.

Fig. 12 displays dual-polarized (HH and HV) dual-frequency (*L*-band at 1.3 GHz and *X*-band at 9.4 GHz) images of a forested area near Ann Arbor, MI. Forested areas are easy to identify on the *X*-band images by their rough image texture; however, they may be easily confused with cultivated crops on *L*-band images because both cover types can produce similar image tones and texture, depending on crop type and growth stage.

c) Polarization variations: When a horizontally polarized wave incident upon a rough soil surface is scattered by the air–soil interface, part of the backscattered energy will have the same polarization as the incident energy and the remainder, usually smaller in magnitude, will be vertically polarized. If the radar has two receivers connected to two antennas, one horizontally and the other vertically polarized, two images can be recorded. These are referred to as HH and HV images, as shown in Fig. 12. Cross-polarized energy can also be generated as a result of volume scattering in inhomogeneous media such as the forest cover in Fig. 12. Being the result of second- and higher order scattering, an HV (or VH) image contains different information about the scattering target from that provided by a like-polarization (HH or VV) image. An example illustrating how multipolarization images can be combined to enhance the discrimination among different target categories is shown in Fig. 13.

IV. Geoscientific Applications of Microwave Remote Sensing Techniques

The intent of this section is to briefly illustrate the manner in which microwave remote sensing techniques are used for geoscientific application in the fields of planetology, meteorology, geology, archaeology, hydrology, and oceanography as well as studies of cultural and natural vegetation.

A. Planetary Applications

In 1978 the Pioneer Venus Orbiter (PVO) went in orbit around Venus. Its payload included a radar mapper which provided low-resolution imagery of the planetary surface and profiles of its topography [40]. The PVO radar operated at a frequency of 1.76 GHz (17-cm wavelength) and used a 38-cm dish mounted on a spinning spacecraft (12-s spin

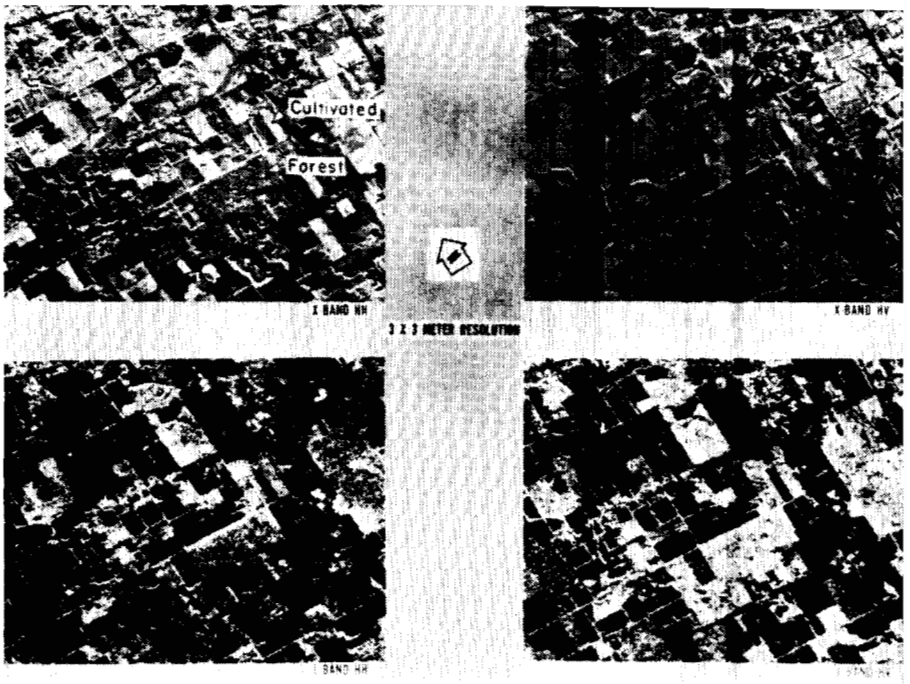

Fig. 12. Dual-frequency dual-polarization images of the Saginaw forest area near Ann Arbor, MI (images courtesy of ERIM).

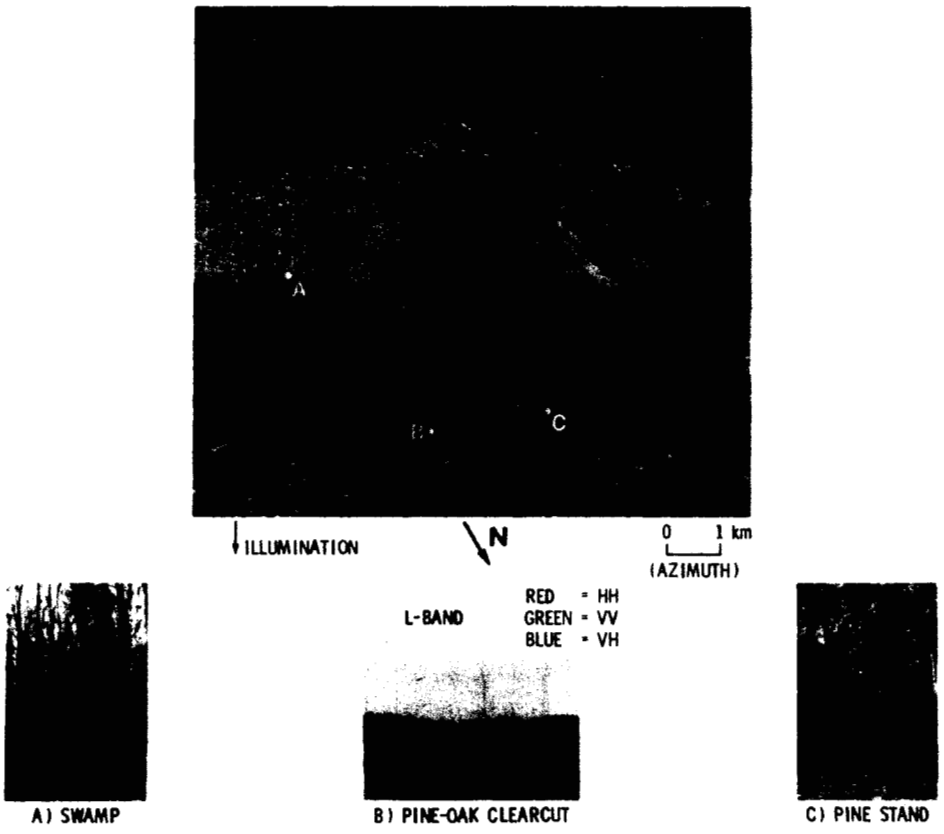

Fig. 13. Multipolarization *L*-band aircraft SAR images of the Savannah River area in South Carolina. Cypress–tupelo association appears pale yellow on the color composite. Distinction of hardwood island (reddish-blue) and marsh on tributary deltas (yellow) in swamp areas is unclear on black and white images. Clearcuts and open water appear dark (image and interpretation courtesy of JPL).

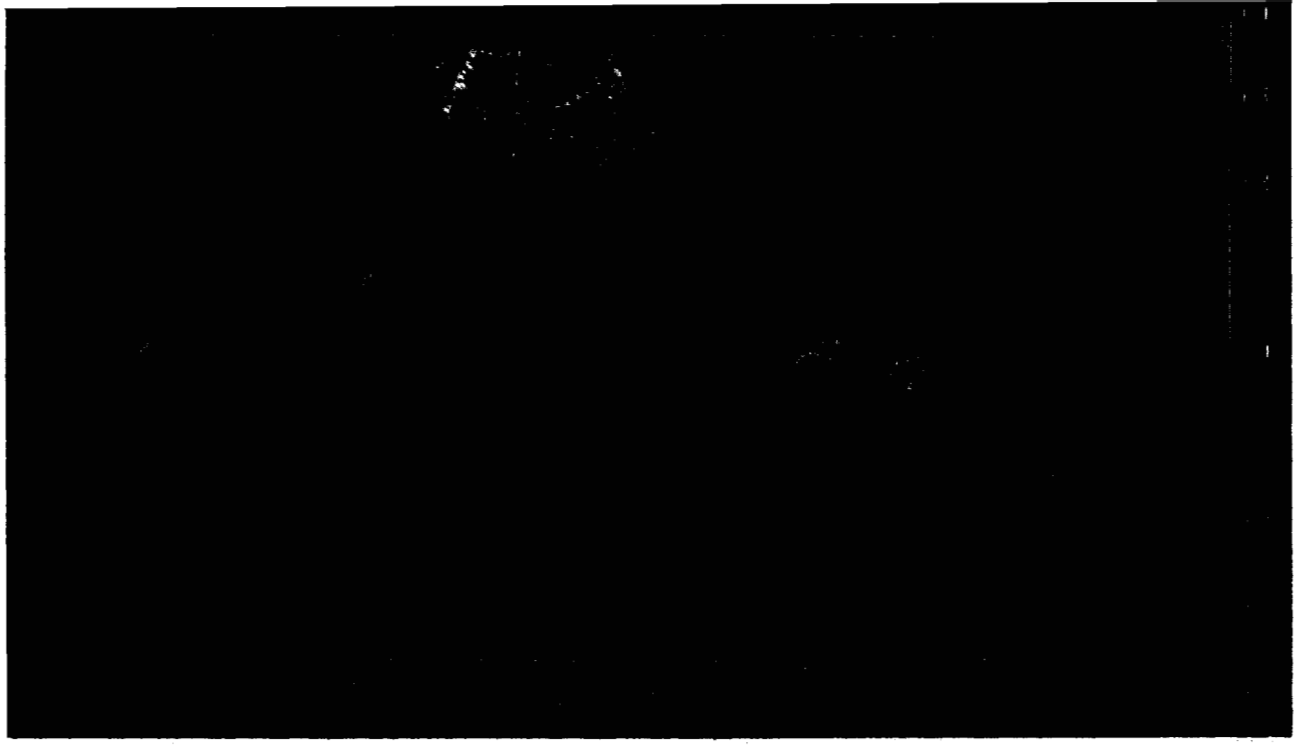

Fig. 14. Global relief map of Venus in Mercator projection. The colors represent constant levels as shown on the right. Shaded relief enhancement has been superimposed to show three-dimensional effect.

period). Fig. 14 shows one example of the data acquired with that sensor. It gives a false-color rendition of the global topography of Venus except for the polar regions. The two main "high" regions are the *Ishtor Terra* and the *Aphrodite Terra*, the latter being spatially larger than South America. Except for prominent elevated features, the planet is quite flat. The highest point observed has an altitude of 11.1 km relative to the median radius of 6051.2 km. The lowest point observed is at −1.9 km.

In 1983, two Russian Venera spacecraft carried SARs which mapped a large portion of the Venusian northern hemisphere with a resolution of a few kilometers. The imagery showed indications of possible tectonic activity on a large scale. Detailed studies of the cloud-covered surface will be conducted with the high-resolution (150-m) global coverage imagery which will be acquired with the US Venus Radar Mapper (VRM) mission in 1988 [41]. The VRM sensor will operate at *S*-band and will also use the synthetic aperture technique.

B. Atmospheric Applications

One of the most important applications of microwave remote sensing techniques has been for both passive and active probing of the atmosphere for both operational and scientific uses. By far the most common operational application is the use of microwave radars for measuring backscatter from rain, clouds, and atmospheric water in meteorological studies and weather prediction. However, lower frequency radars are also useful. By using HF (3–30 MHz), VHF (30–300 MHz), and UHF (300 MHz–3 GHz) radars to observed scattering from turbulence-induced refractive index fluctuations, for example, it is possible to measure atmospheric winds and detect clear-air turbulence for improved weather prediction and aircraft routing [42].

Passive microwave radiometers are particularly useful in meteorological and climatological applications, for such measurements as atmospheric temperature profiles, global water-vapor distribution, precipitation, and sea-surface winds. The Nimbus-5 satellite launched in 1972 carried the 19.3-GHz Electronically Scanned Microwave Radiometer (ESMR) which for many years provided 25-km resolution images of water vapor and precipitation over the ocean; the Nimbus-5 NEMS, in addition to providing nadir views of water vapor, sounded temperatures at nadir in three 8-km-thick atmospheric layers centered at 4, 11, and 17 km. The Nimbus-6 SCAMS was similar to ESMR except it operated at 37 GHz; it provided the first space images of water vapor and precipitation, as well as atmospheric temperature fields. The success of the results obtained from the Nimbus-6 research satellite led to the inclusion of a four-channel Microwave Sounding Unit on the Tiros-N weather satellite launched in 1978. In 1978 two satellites, Nimbus-7 and Seasat, carried aloft the Scanning Multichannel Microwave Radiometer (SMMR) instrument for observations of atmospheric rain rates, water vapor, and liquid water; SMMR used five frequencies between 6.6 and 37 GHz. (See Table 1 for more information on ESMR, NEMS, SMMR, and SCAMS.)

The temperature accuracies of these microwave sounders and imagers are of the order of 1° to 5° depending on altitude, latitude, and season. The addition of more channels would improve the accuracy. Satellite radiometric mea-

integrated value, and have typical accuracies of a few percent [43].

Further exploitation of satellite microwave radiometers for meteorological research and operational weather satellites will require the addition of more channels which can measure atmospheric molecular constituents such as O_3, H_2O_2, and CO at frequencies extending even above 200 GHz.

For a discussion of the scientific basis for using passive microwave radiometry in meteorology and climatology, the reader is referred to papers by Staelin [19], [44]. An excellent survey of the results obtained from SMMR, NEMS, SCAMS, and other satellite radiometers is provided in the Njoku paper [3].

C. Geological and Archaeological Applications

Images from spaceborne remote sensors provide a synoptic regional view of the earth's surface. They are used to detect, delineate, map, and identify features, patterns, shapes, albedo variations, texture variations, and their relative spatial relationships on a regional and continental scale. Visible and near-IR images of the earth's surface acquired or flyby satellite cameras, have been extensively used since the late 1960s for geologic mapping. More recently, radar images acquired with Seasat, SIR-A and SIR-B have been used for similar and complementary studies (for examples, see [1], [45]–[51]).

Visible and near-IR sensors provide information about the surface properties by using the reflected solar radiation. In this case, the surface albedo (e.g., reflectivity) is mainly a function of the chemical composition and slope of the surface or the top of its cover. Because of the short wavelength of the illuminating radiation (fraction of a micrometer to a few micrometers), the electromagnetic wave can probe only the top few micrometers of the surface layer. Thus any vegetation, sand, alluvium, snow, or desert varnish cover would limit the capability to map the underlying surface.

Radar sensors use wavelengths in the range of a few centimeters to a few tens of centimeters. As discussed earlier, this allows probing of up to a few meters through the surface cover (see Fig. 9). The surface albedo is mainly a function of the surface slope and roughness, and the dielectric constant and volumetric inhomogeneities of the near-surface layer.

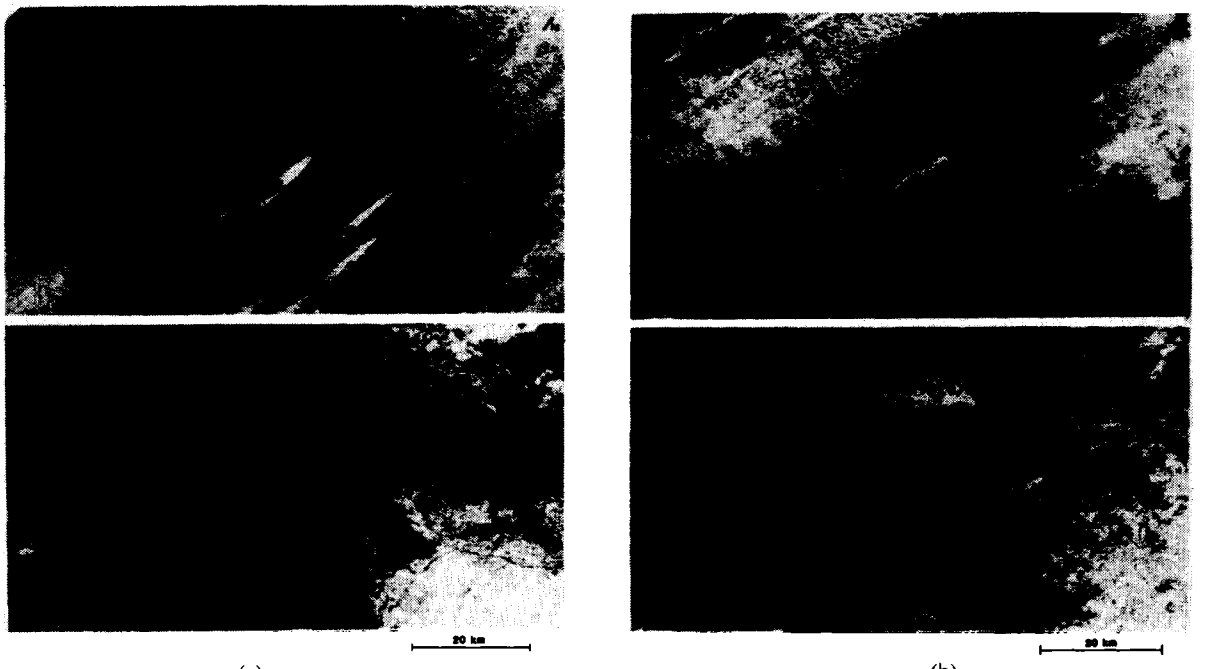

(a) (b)

Fig. 15. (a) SIR-A (bottom) and Landsat (top) images of a 50 × 100 km area of the Egyptian–Sudanese border. The Landsat image shows a landscape dominated by aeolian processes. The Selima sand sheet blankets the underlying material with windblown sand to a few meters thickness. Presently, active dunes marching across the sand sea are visible as the diagonal streaks near the image center. In contrast, the SIR-A image reveals a landscape carved by fluvial processes, now buried beneath the sand. The confluence of what were two large rivers is shown in the center of the SIR-A image. Note that the dunes in the Landsat image have no expression on the SIR-A image. SIR-A image from data take 28, rev 27, acquired November 14, 1981. Landsat band 6 image, November 11, 1972. (b) SIR-A (bottom) and Landsat (top) images of an area in southwestern Egypt. Once again, the Landsat image primarily shows a landscape dominated by aeolian processes, with dunes and the sand sheet forming most of the visible features. The SIR-A image reveals fluvial landforms buried by the sands. Note in particular the braided stream channels near the top of the SIR-A image. The line on the Landsat image is a slight break in the mosaic, the effect of which is heightened by the disparate sun angles. SIR-A image from data take 28, acquired November 14, 1981. Landsat band 6 image November, 1972 (left) and February 9, 1973 (right) (images courtesy of R. Blom, JPL).

unambiguously observed in a number of arid regions: southwestern Egypt [1], [52], northeastern Sudan, and southern California [49]. Covered morphologic features were mapped through a sand cover of up to a few meters (Fig. 15). In actuality, the presence of the cover tends to enhance the capability to detect the subsurface features due to refraction at the surface, as long as the cover is thin and of low loss [52]. In all the cases where penetration was observed, the surface moisture was less than 1 percent volumetric or less than 0.02 g · cm^{-3}. As shown in Fig. 9, this is consistent with penetration depth in excess of 1 m at *L*-band frequencies.

The ability to image buried morphological features has potential archaeological applications. In the case illustrated in Fig. 15, buried old drainage channels were mapped providing information about the hydrological history of the region and indicating that the present extremely arid environment is only recent. Radar images of the area are being used by anthropologists to help identify areas for future exploration, the logic being that past inhabitation would have been concentrated along river banks and shores.

In the case of vegetation cover, surface probing could occur as a result of scattering in the vegetation canopy and reflection at the surface [53]. This is possible in the case of low vegetation density. In the case of heavy vegetation cover, the return will be mostly from volume scattering in the canopy.

In addition to the unique ability to penetrate dry surface cover and tenuous vegetation layers, radar imaging data are particularly useful in structural and morphological mapping because of the strong sensitivity of the radar backscatter to changes in the surface slope and roughness. Fig. 16 shows some examples of images acquired recently with SIR-B of a number of geological features.

Spaceborne radar imagery has also been used in a stereo configuration to generate topographic contour maps. SIR-A imagery of the island of Cephalonia (Greece) acquired from two look directions were used by Kobrick *et al.* [54] to generate 100-m contour maps of the island (Fig. 17). SIR-B acquired imagery at multiple incidence angles over a number of geological regions in order to demonstrate the relationship between the incidence angle, convergence angle, and resulting topographic accuracy.

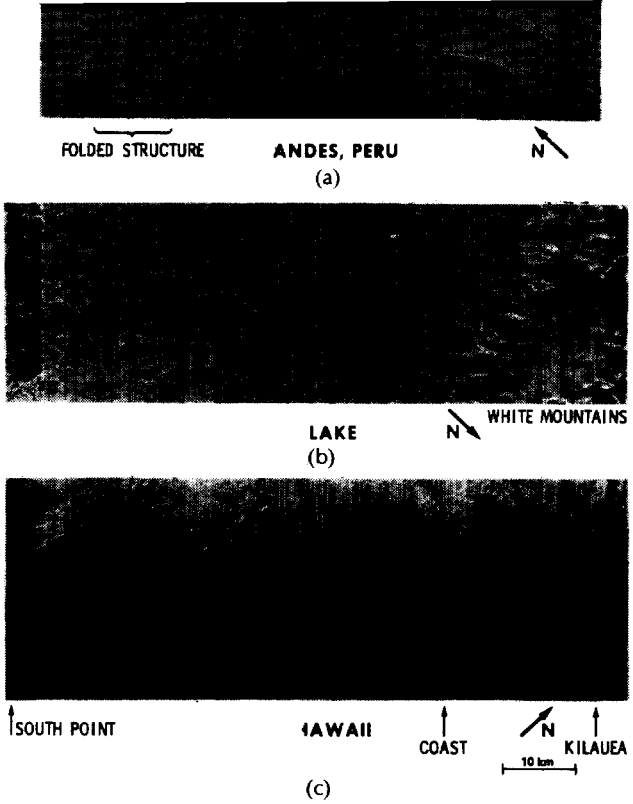

Fig. 16. Radar images of a variety of geologic surfaces acquired with SIR-B in October 1984. (a) Folded, layered rocks of the Paleocene Age (20 million years old) in the high plateau of northern Peru show extreme dissection and local offsets of the rocks due to faulting. At the center of the image is the Maranon River which is a major tributary of the Amazon. Radar incidence angle is 55°. The image is approximately 15 km × 15 km. Location is 4°54′ S and 78°20′ W. (b) Glacially sculpted terrain in New Hampshire and southwestern Maine. The image is centered on Ossipee Lake (43°48′ N, 71°09′ W). Ossipee Mountain is the large circular feature above Ossipee Lake. At the right is the Sandwich Range of the White Mountains. The radar incidence angle is 34°. (c) Volcanic terrain along the southeastern coast of the island of Hawaii. Lava flows, cinder cones, and calderas are clearly visible. At right is the Kilaweia crater. Radar incident angle is 28°.

D. Hydrological Applications

An understanding of the water resources in an area requires an assessment of the hydrologic cycle factors of precipitation, runoff, infiltration, irrigation, evaportranspiration, etc. Hydrologic processes can be viewed as space–time phenomena, although models currently used to evaluate these hydrologic factors mainly rely on point–time data. Moreover, design and planning procedures based on these point data sources have not changed very much in the past twenty to thirty years.

Remote sensing techniques, including microwave remote sensing methods, offer the potential to provide distributed data leading to space–time hydrologic information. Satellite remote sensing data are especially useful for describing drainage networks, topography, soil type, soil moisture, snowpack extent, runoff coefficients for small watersheds, etc. Thermal IR and passive microwave measurements by NOAA/Tiros-N (atmospheric water vapor and temperature profiles), Nimbus-7 (surface temperature), and HCMM (albedo) have been used for evaportranspiration estimates. Landsat TM data have been used for high-resolution surface water observations allowing inventory of smaller bodies of water, improved flood plain delineation, etc.

Microwave remote sensing at *L*-band or *C*-band is particularly promising as a technique for surface water mapping, soil moisture monitoring, and for observation of surficial geometry, roughness, and slope. Surface water maps are important in water resource management, and the lower microwave bands are well-suited to observation of surface water extent because of their increased penetration of vegetation. The spatial and temporal distribution of soil moisture is a key input parameter to meteorological, hydrological, and crop yield models. Because of the strong dependence of the soil's dielectric constant on its moisture content, *L*-band or *C*-band radars and radiometers are very useful for monitoring soil moisture.

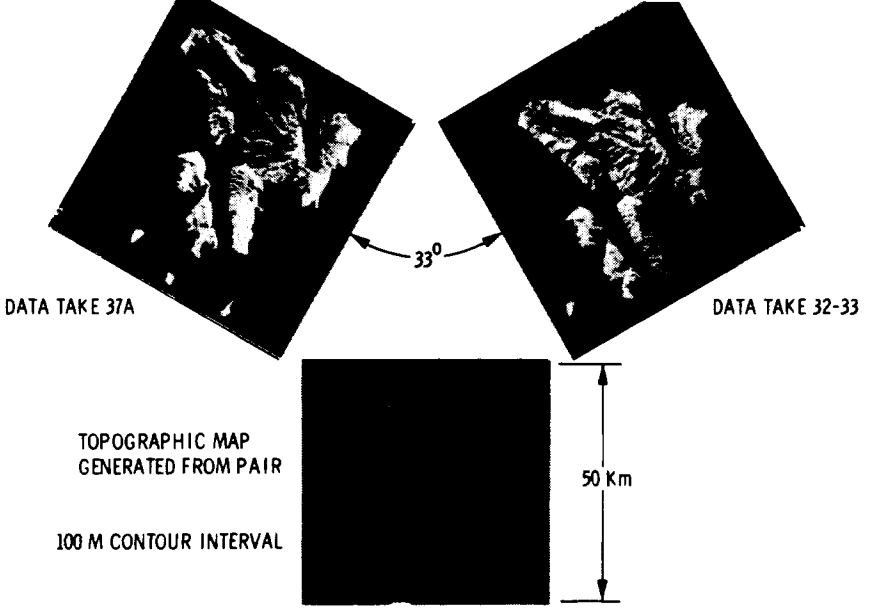

Fig. 17. Stereo pair images of the island of Cephalonia in Greece, acquired with SIR-A in 1981. The angle of convergence is only 5°. This still allows stereo observation.

From satellite altitudes, a SAR can achieve a resolution of the order of tens of meters, and can provide high-resolution imagery for hydrologic information. A satellite *L*-band radiometer can achieve a resolution of the order of a few kilometers and thus provides moderate-resolution imagery. For moderate-resolution regional or global observations of hydrologic features, an *L*-band radiometer using a 50–100-m diameter antenna would be useful although an instrument of this size has not yet been tested from space. (The Skylab S-194 *L*-band radiometer launched in 1973 had a small antenna and a relatively coarse resolution of 115 km.)

Many hydrologic applications such as runoff prediction, crop-yield predictions, irrigation scheduling, etc., require high-resolution information over large areas of the earth and for this a spaceborne SAR is needed. Extensive research has been conducted over the past decade to define optimum radar specifications for soil moisture estimates on a regional scale [39], [17]. Seasat, SIR-A and SIR-B images, all at *L*-band, have been used to study sensitivity to soil moisture. For the false-colored Seasat SAR image shown in Fig. 18(a), for example, the blue-colored areas in the eastern portion of the image—which corresponds to a high radar-return level—represents high soil moisture conditions resulting from precipitation on the eastern portion (Fig. 18(b)) on the day prior to the Seasat overpass.

Radar remote sensing techniques also have the potential for monitoring snow pack dynamics. Most of the research conducted to data [37], [55], [56], however, has been limited to scatterometer measurements and theoretical modeling of the dependence of σ° on snow water equivalent (the total amount of snow water contained in a vertical column) and snow wetness (liquid water content). Nevertheless, the results indicate that radar is very sensitive to changes in snow wetness, and that it may be possible to monitor changes in water equivalent through the detection of changes between successive observations.

E. Vegetation

Living organisms along with their physical and chemical environment are bound inseparable parts of a biogeochemically active earth whose recycling elements are driven by the forces of solar radiation, biological activity, and thermal processes within the mantle and core. Over the past few decades, humans have significantly disturbed the natural carbon and nitrogen cycles in the biosphere to the point that a global study of the biosphere has become one of the major scientific challenges of the next decade. An understanding of biological productivity requires improved knowledge of energy budgets, hydrologic cycle, other biogeochemical cycles, and couplings between these processes. The spatial distribution and temporal dynamics of biological productivity on land are keys to an improved knowledge of biological interactions with energy, hydrology, and other biogeochemical cycles [57], [58].

Remote sensing from space offers the potential to analyze major biogeochemical processes including carbon, nitrogen, sulfur, and phosphorus cycles on global and regional scales. Quantitative estimations of the pools and fluxes of vegetation biogeochemical elements can be made by knowing the structural characteristics of vegetation. Vegetation structural indicators such as leaf area index (LAI), total biomass accumulation (TBA), and net primary productivity (NPP) are of particular interest [59]. The net primary productivity (NPP), i.e., the amount of photosynthate produced per incident photon energy, depends on the amount of photosynthetic light in the visible wavelength range that falls upon the plant and, of course, on the plant species. The quantity of solar energy intercepted by a plant depends upon both the total leaf area and on the foliage angle as well as plant geometry. The LAI is the surface across which photosynthesis is supported through the exchange of energy, oxygen, and carbon dioxide, and the surface across

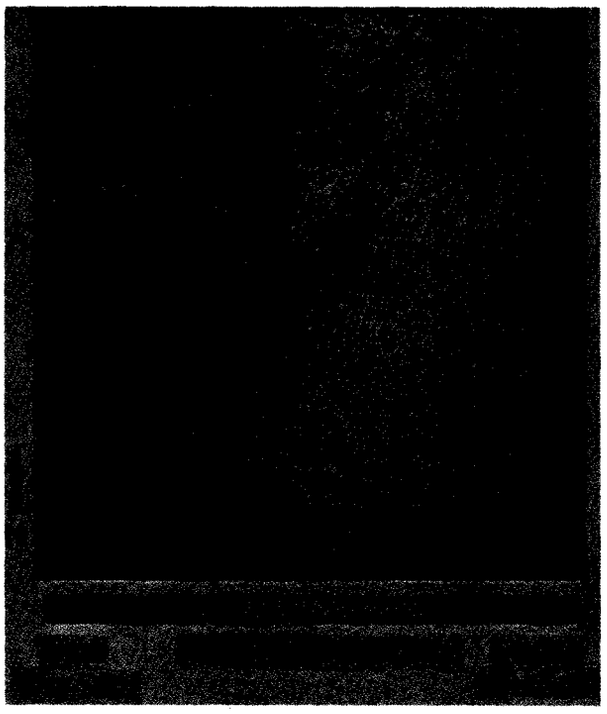

(a)

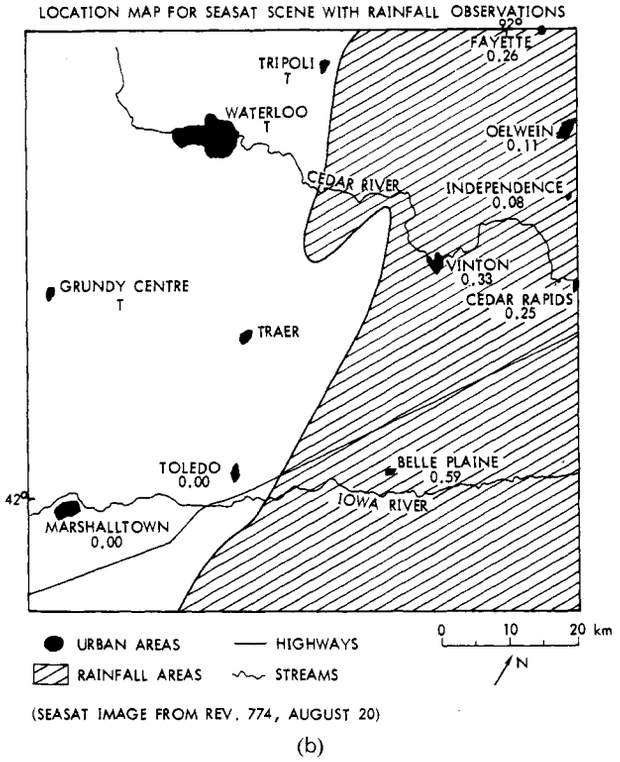

(b)

Fig. 18. Color-enhanced Seasat SAR image delineating rainfall extent over central Iowa (a) and the corresponding location maps (b) for rainfall observations. Light blue color represents areas that received significant rain on the day prior to the Seasat overpass. The green and orange colors represent areas with relatively dry soil conditions. The color coding was generated on the basis of the image intensity of the original SAR image (Ulaby *et al.*, [17]).

which water is transpired for plant maintenance [60]. LAI can range from near zero to about 23.

Remote sensing techniques allow the estimation of biological productivity through the observation of LAI, plant morphology, soil moisture, and soil temperature. Each part of the spectrum (visible, near-IR, thermal IR, and microwave) provides unique information about the plant community and its soil background. Microwaves backscattered from vegetation canopies, both natural and cultural, are particularly sensitive to the geometrical structure of the plants, and the backscatter coefficient σ° is sensitive to a wide range of LAI values. As would be expected, the backscatter coefficient varies markedly over the growing season of a vegetation canopy.

In order to illustrate the potential use of radar for monitoring cultural and natural vegetation, three examples are presented. The first example relates to a crop classification study. A 9.4-GHz real-aperture airborne imaging radar was used to obtain multidate images of an agricultural test site in The Netherlands [61]. Fig. 19(a) shows a color image generated by color-combining three radar images corresponding to the dates indicated. On single-date images, only 30 percent of the fields (consisting of 182 fields comprising seven crop types) were correctly identified. However, when data from three dates were used together, the accuracy improved to 88 percent (compare parts (b) and (c) of Fig. 19).

The second example, Fig. 20, shows the temporal variation of the backscattering coefficient σ° for a field planted in wheat; the data cover a period of about three months extending from shortly after emergence until harvest. Analysis of these and other data has shown that σ° can be related to the LAI of the wheat canopy, as shown in Fig. 21.

The last vegetation example is related to the use of radar for forest inventory. Shuttle Imaging Radar (SIR-A) images acquired over Baldwin County, AL, during two shuttle passes in November 1981 were used by Wu [62] to evaluate the degree of separability between different classes of pine forest achievable on the basis of radar imagery. Fig. 22 shows histograms for three pine forests. The order of the distributions along the digital-number axis indicates that the radar scattering coefficient of a forest canopy generally increases with increasing canopy height.

F. Polar Ice

Microwave remote sensing techniques are crucially important to improving our knowledge of sea ice and ice sheets for both scientific studies of the polar regions and operational applications for polar marine navigation, coastal petroleum exploration, etc. Because of the extreme difficulty and cost of carrying out surface observations, coupled with the problem of cloud obscuration of Landsat imagery, relatively little is known about polar geophysics. It is known that many polar ice processes occur over large spatial scales and can change markedly in a matter of days. It is also known, of course, that during the winter sea ice grows in thickness and extent and that during the summer melt season it contracts. However, the processes of ice expansion and contraction are very different in the two hemispheres. The area of new pack ice formed each winter in

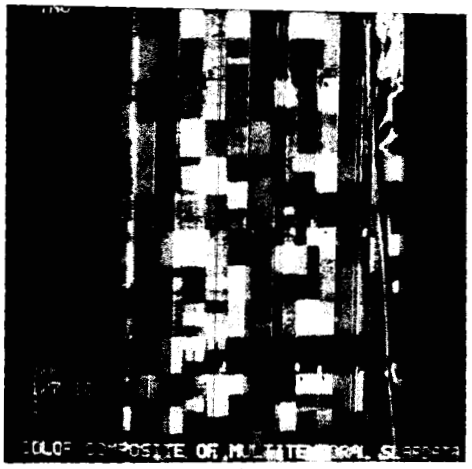

(a)

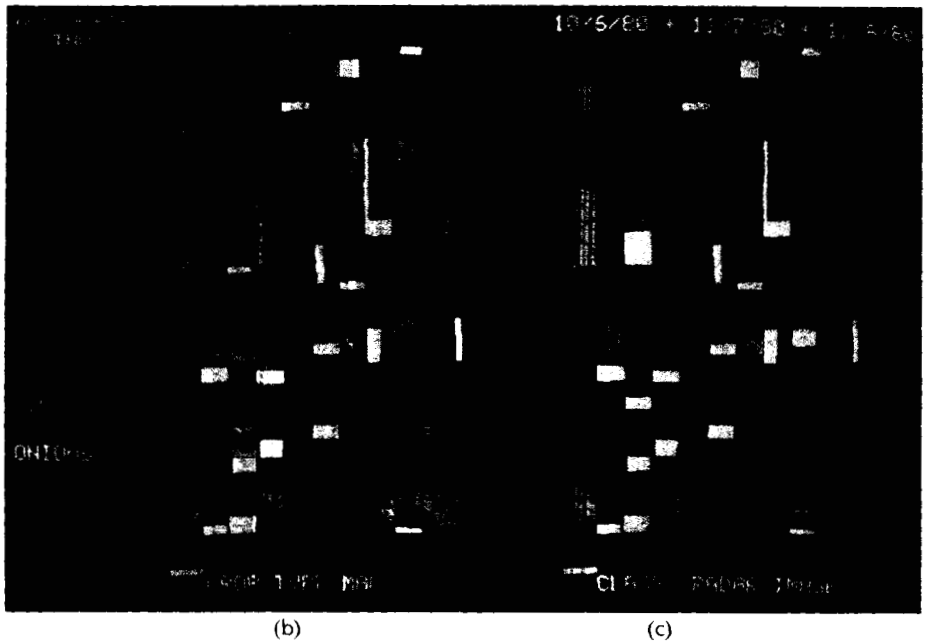

(b) (c)

Fig. 19. Crop classification with multidate observations by *X*-band SLAR. (a) Color composite of three SLAR images. (b) Crop type map. (c) Crop type as classified by the radar image-composite shown in (a) (images are courtesy of Hoogeboom; see Hoogeboom, [61]).

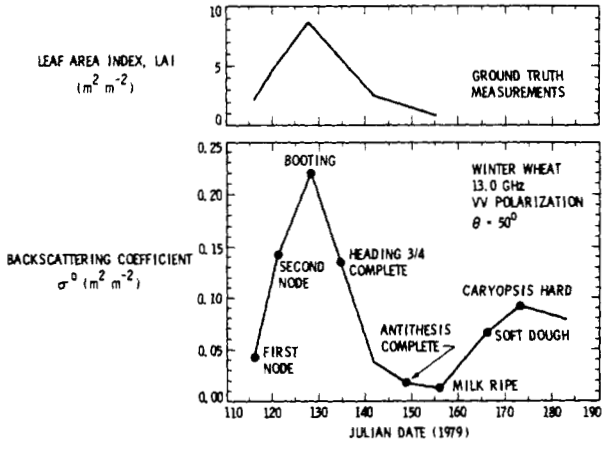

Fig. 20. Measured temporal patterns of the backscattering coefficient σ° and the leaf area index (LAI) for a winter wheat field in Kansas [Ulaby *et al.*, [18]).

the Antarctic Ocean is considerably larger than the entire Arctic Ocean area. Moreover, very little Antarctic pack ice survives during the summer while the central Arctic Ocean pack ice remains throughout the year.

Both short-term weather predictions and longer term climate forecasts require an improved understanding of the extent to which sea ice alters atmosphere–ocean exchanges of heat, moisture, and momentum. Existing dynamic and thermodynamic pack ice models suggest that the Arctic ice pack may respond dramatically to a general warming, and improved models and data are needed. The Antarctic and Greenland ice sheets are also important to the climate system and contain about 80 percent of all the fresh water on earth. The complete melting of these sheets would raise the earth's oceans by 65 to 70 m and even a small warming could raise the sea level substantially [63]. In addition to these scientific questions, the increased demand for the exploitation of polar region natural resources such as petro-

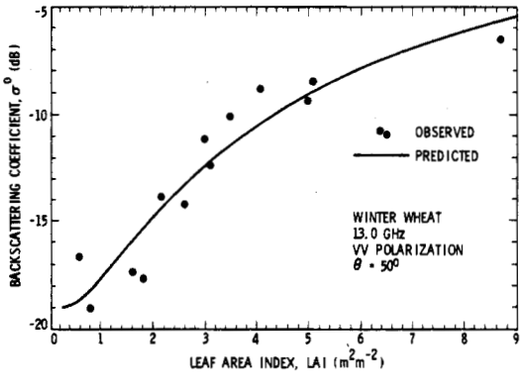

Fig. 21. Variation of radar backscattering coefficient with LAI for LAI > 0.5 (Ulaby *et al.*, [18]).

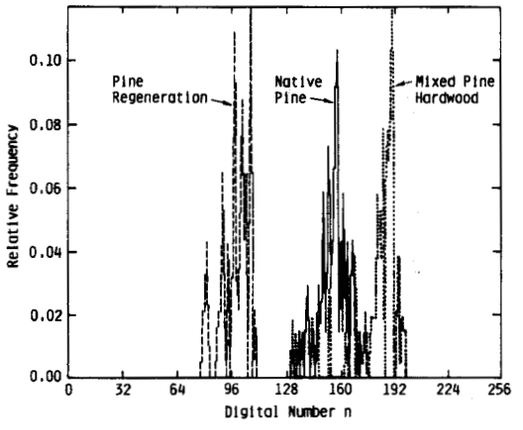

Fig. 22. Histograms of three pine forests, based on a SIR-A image of Alabama (from Wu, [62]).

leum, minerals, and fresh water requires improved predictions of sea, lake, and river ice extent and movements for shipping and offshore petroleum exploration, better short-term weather predictions and real-time observations of the character and distribution of first-year and multiyear pressure ridges, multiyear floes, ice islands, etc.

An improved understanding of these processes requires more information about both the dynamics (sea-ice motion) and thermodynamics of the polar ice regions. Because of its ability to produce high-resolution (approximately 30 m) all-weather cloud-free images, a wide swath spaceborne SAR is an ideal tool for the study of sea-ice dynamics. On the other hand, a satellite imaging radiometer can provide valuable information on the thermodynamic processes of sea ice by mapping at moderate resolution (approximately 30 km) and at regular intervals over the season the area of open water within pack ice and ice characteristics such as age, thickness, roughness, etc. Scatterometers are also useful for the study of ice characteristics. Because the dynamic and thermodynamic processes are related, it is highly desirable to have simultaneous radar and radiometer coverage of the polar regions.

Since 1969, a number of major ice remote sensing expeditions and missions have been conducted in which coordinated surface, aircraft, and satellite observational programs have tested passive and active microwave remote sensing instruments and techniques. Some of the most useful satellite radiometric imagery was obtained by ESMR (Electronically Scanned Microwave Radiometer operating at 19.3 GHz) launched on Nimbus-5 in December 1973. ESMR provided 30-km resolution images of the Arctic and Antarctic regions which, during its four-year lifetime, permitted numerous geoscientific breakthroughs in our knowledge of sea ice and ice sheets. ESMR images were used to distinguish sea ice from water, multiyear ice from first-year ice, and ice type ratios. Fig. 23 shows ESMR passive microwave images of the Antarctic polar region during both the winter and summer, and dramatically illustrates the ability of the sensor to map sea ice seasonal expansion and contraction [63]. Thus passive microwave imagery from satellite altitudes is extremely useful for thermodynamic studies of sea ice.

The first extensive set of spaceborne SAR images of Arctic Sea ice structure and dynamics was provided by Seasat during the summer of 1978. More than 100 passes over the Beaufort Sea were recorded on an essentially daily basis, allowing the first studies on major morphological features, structural changes, and sea-ice drift motion [64].

When sea ice is formed, it is relatively thin and has a smooth surface. After this initial formation, however, the ice undergoes compressive and shearing forces from the

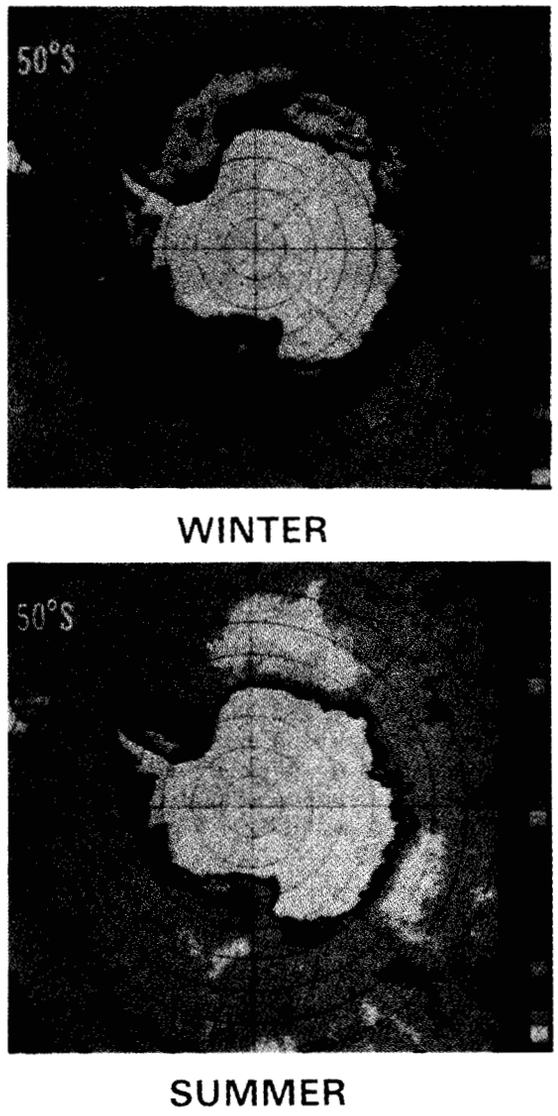

Fig. 23. ESMR passive microwave images of the Antarctic polar region. (a) Winter, showing extent of pack ice. (b) Summer, showing greatly contracted size of pack ice.

motion of other ice floes, surface currents, and wind stresses as well as temperature fluctuations, resulting in marked structural changes in the ice features such as pressure ridges, and increased thickness and surface roughness. Thus some SAR image discrimination between first-year and multiyear ice can be made on the basis of surface roughness and shape. However, the primary advantage of SAR imagery is to allow detailed studies of sea ice dynamics. As an example, Fig. 24 is a Seasat image in which a small ice island entrapped in the main Beaufort Sea ice pack can be seen as

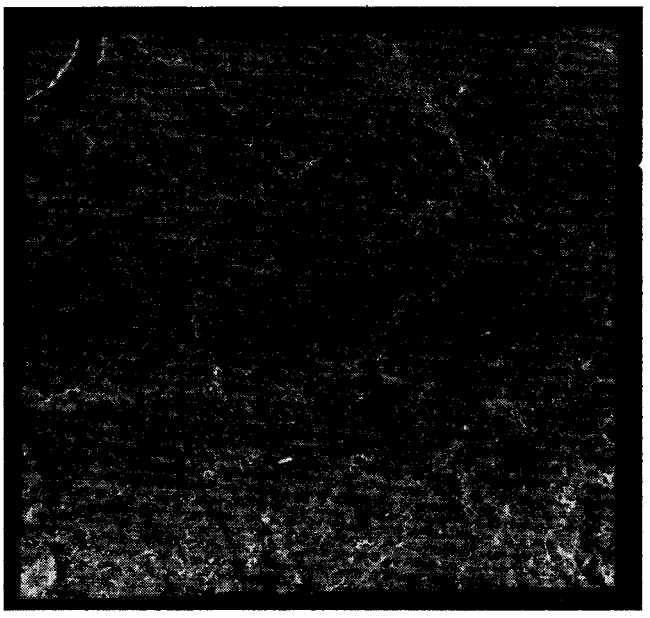

Fig. 24. Seasat SAR image of a region in Beaufort Sea, showing small ice island entrapped (at 6 o'clock, 2/3 way down from center).

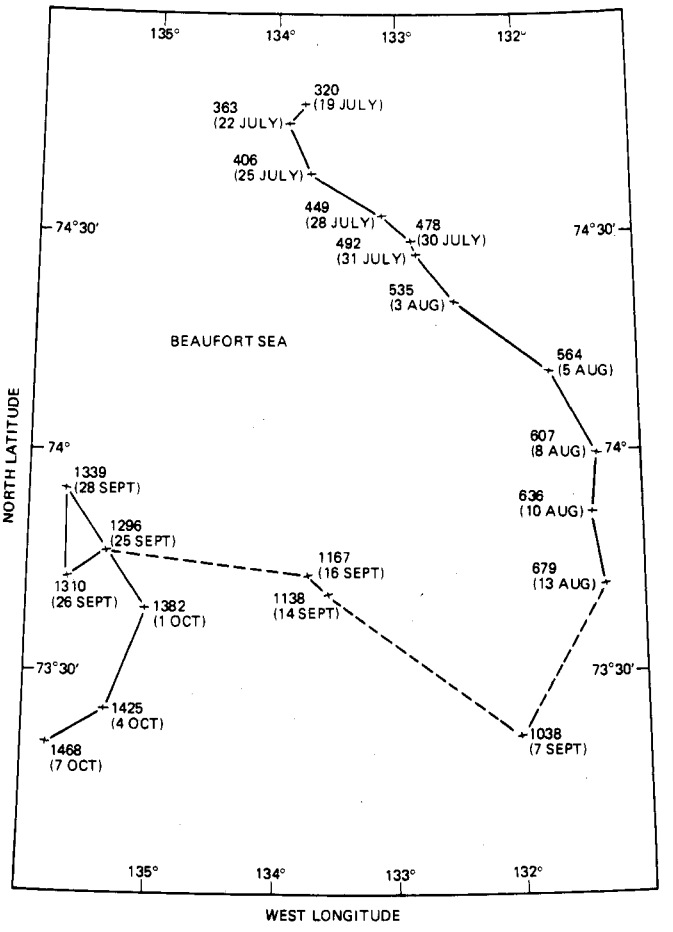

Fig. 25. Drift path of island from July 19, 1978 to October 7, 1978 as obtained from Seasat images.

a bright anomalous feature up from the bottom center of the image. This feature was imaged by the Seasat SAR on 20 separate passes, providing an opportunity to study the drift of an ice island within pack ice. Fig. 25 shows the drift path of the island over the period from July 19, 1978 to October 7, 1978. Similar SAR imaging techniques can be used to study other dynamic properties of sea ice, including the motion of ice floes.

Satellite-borne radar altimeters are useful for mapping changes, as was first demonstrated by the GOES-3 altimeter launched in 1975. The GOES-3 altimeter data were used to map the southern Greenland ice sheet topography with significantly improved accuracy over earlier measurements [65]. Altimetric data are important for the development and testing of numerical models of ice sheet dynamics, although long-term data sets (3–5 years) are needed.

The optimum incidence angles and frequencies for radar remote sensing of sea ice are not known with certainty, despite recent field and aircraft experiments conducted at frequencies from *L*-band through *Ku*-band. One problem of considerable interest is the optimum combination of incidence angles and frequencies for distinguishing ice type (thin first-year ice, thick first-year ice, multiyear ice, pressure ridge ice, etc.). Currently available data suggest that it is difficult to discriminate between first-year and multiyear ice at the lower microwave frequencies and that frequencies above *X*-band are necessary for improved discrimination.

G. Oceans

The principal objectives of satellite remote sensing for investigating oceanic physical processes are to acquire global coverage of such mesoscale surface features as surface stress, ocean topography, sea-surface temperature, and sea-ice characteristics and dynamics. *Surface wind stress* is a major driving force of large-scale oceanic circulation, and represents the lower boundary condition for models of the atmospheric circulation over the ocean. The topography or hills and valleys of the ocean's surface are related to ocean bottom topography, surface currents, eddies, and other features of ocean circulation, so that if *ocean topographic* maps can be made, the details of ocean circulation will be evident as well as major ocean bottom morphological features. The *sea-surface temperature* is a measure of the upper ocean layer heat content and is a very important factor in the exchange of heat energy between the atmosphere and the ocean. In addition to these earth system scientific questions, satellite remote sensing of the oceans provides information of interest to shipping, fisheries, weather, etc.

Microwave remote sensing of the sea surface from space has the greatest potential for geoscientific information because of the uniquely sensitive nature of these longer wavelengths to centimeter to decimeter ocean wave features and temperature while penetrating clouds.

Passive imaging radiometers are very useful in the mea-

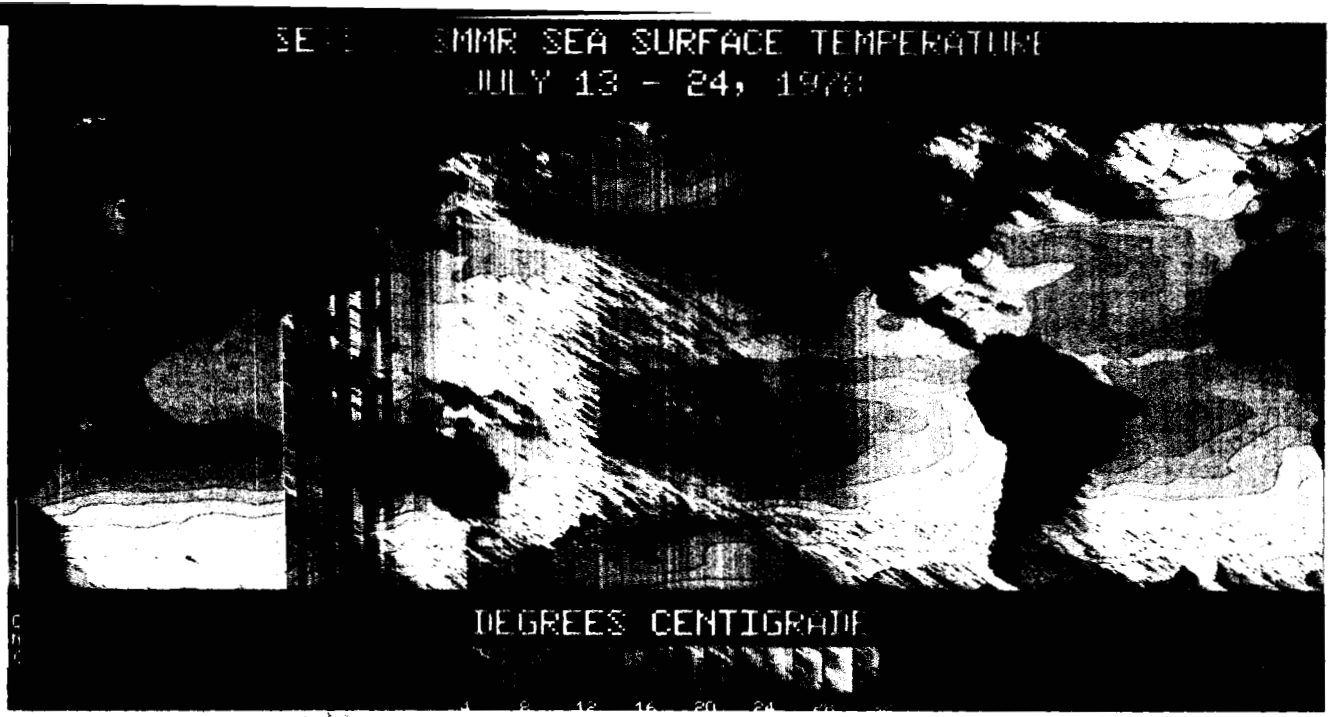

Fig. 26. Nimbus-7 SMMR global sea temperature map.

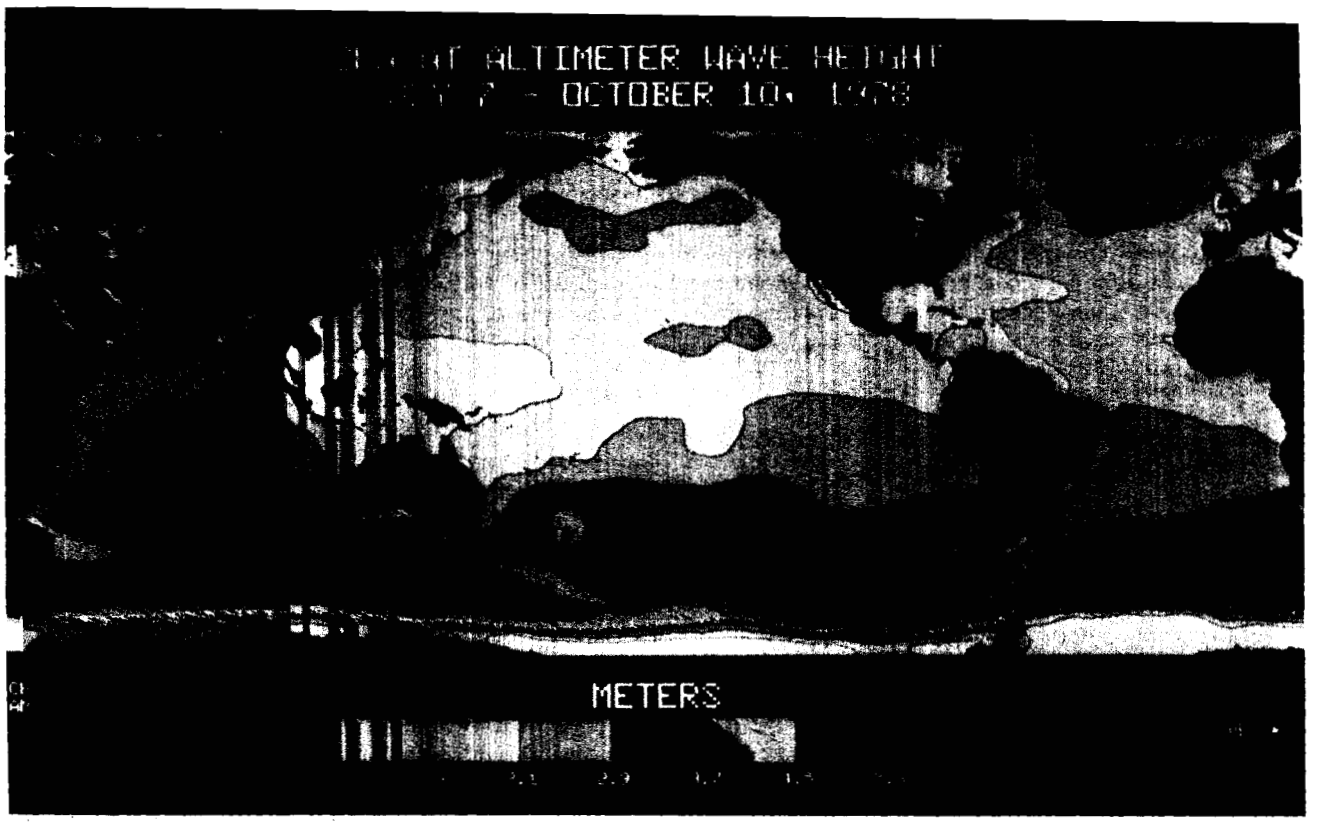

Fig. 27. Seasat altimeter map of global wave heights. [74].

surement of both sea-surface temperature and sea-surface salinity without being hampered by cloud cover. The five-frequency SMMR on Seasat launched by NASA in 1978 has been used to produce sea-temperature maps to within an accuracy of about 1.3°C and a resolution of 150 km [66], as shown in Fig. 26. Aircraft tests have shown that a space-borne *L*-band imaging radiometer could measure sea-surface salinity in very fine gradations of 500 parts per million [67], [68].

The 13.5-GHz altimeter flown on GOES-3 and later on Seasat provided a convincing demonstration of the useful measurements of ocean topographic features that could be made from satellite altitudes [69]. Fig. 27 shows a global wave-height map obtained from the Seasat altimeter. The

precision of the Seasat altimeter was approximately 5 cm, although a number of corrections must be applied to the apparent altimetric height such as the amount of atmospheric water vapor, the number of ionospheric free electrons, and the uncertainty in the knowledge of orbit due to the geoid. This geoidal uncertainty can range from less than a meter up to 10 m.

A very important task of remote sensing is to measure oceanic winds at global scales. The Seasat mission showed that both scatterometers and SARs are useful for this purpose. The 14.6-GHz Seasat scatterometer was used to determine wind speed to an accuracy of about 1.3 m/s. The direction estimated from Seasat scatterometer data for the wind velocity vector has inaccuracies due to aliasing. The physical basis for scatterometric observations of sea surface winds is the Bragg scattering of 2-cm wavelength microwaves by centimeter-long ocean waves. An X-shaped illumination pattern was used to first view a given surface location by the forward-pointing antennas and a few minutes later by the aft-pointing antennas. The scatterometer data were processed to give a normalized radar cross section from which wind speeds were determined from a lookup table [2].

Images of the ocean recorded by the Seasat SAR showed a great variety of ocean surface features including long ocean gravity waves, internal waves, and indirect evidence of ocean bottom morphology, entrained substances, etc. [70]. It is generally presumed that the mechanism for Seasat imaging over the open ocean is the Bragg scattering from gravity waves with tens of centimeter wavelengths, although there are still important unanswered questions. Nonetheless, SAR imagery obtained by Seasat as well as by SIR-A and SIR-B have demonstrated that spaceborne SAR can yield global information on surface wind magnitude and direction, the spatial evolution of storm wave patterns, spatial distribution of internal waves, ocean fronts and eddies, as well as long-term changes in bathymetry and the marginal ice zone. The directional spectrum for both winds and ocean waves can be extracted from Seasat SAR data [71].

V. Technology Developments, Future Sensors and Missions

A. Technology Developments

Future earth observation missions will routinely include both radars and radiometers in thier instrument clusters, both for the unique information available in the microwave spectrum and for the synergism of microwave data with thermal IR, near-IR, and visible data. The nature of information required for studies of the earth as a system places new demands on the performance of the next generation of microwave radars and radiometers, particularly for images which are both timely and calibrated. These instruments will be operated on various platforms in polar, near-equatorial, and geosynchronous orbits and with lifetimes ranging up to several years.

1) Calibration: A central issue for both radars and radiometers is calibration, both absolute and relative. For a SAR, it is desirable to achieve a relative calibration (short- and long-term stability) of a few tenths of a decibel and an absolute calibration of the order of 1 dB. For a scatterometer used in the measurement of the Bragg scattering from centimeter-wavelength gravity and capillary waves, the required absolute calibration is less than 1 dB. An imaging *L*-band radiometer used for the measurement of sea surface salinity would require an absolute calibration of about 1 K and a sensitivity and stability of approximately 0.05 K. These calibration levels are feasible on a short-term (many month) basis, although it has not been demonstrated that they can be reached for a many-year satellite lifetime.

2) Future Radiometer Challenges: Although the technology problems facing future spaceborne imaging radiometers are perhaps not as severe as those involved with SARs, they are still quite challenging. A very high priority development in the meteorological community is a 20-channel microwave radiometer for spaceborne imaging of both atmospheric water vapor and atmospheric temperature profiles; this would involve frequencies from about 6 up to 200 GHz which would be used to observe various atmospheric molecular constituents. This would require the development of low-noise radiometers for the higher frequency channels, high-efficiency antenna clusters, etc. Another proposed system is the Shuttle Large Area Multichannel Microwave Radiometer (SLAMMR), which would use a 4-m-diameter offset-fed parabolic reflector antenna on the Shuttle. This antenna could be deployed in space and mechanically scanned by rotating at the rate of 1 rev/s, thereby sweeping out a constant-incidence angle conical surface along its ground track. Other proposed future configurations include a multibeam pushbroom *L*-band radiometer for sea-surface mapping, although the technology to accomplish this is essentially in place. Spaceborne radiometers, although producing comparatively modest resolutions, require very small prime power, have low data rates (order of kilobits per second), and do not require complex image processors.

Almost invariably, the most difficult problem in an imaging spaceborne radiometer is the antenna. At the lower microwave frequencies, the problem is principally the physical size. For example, an *L*-band imaging radiometer with even a 1-km resolution from a 400-km altitude requires an antenna diameter of about 90 m. At the higher frequencies (e.g, 19–7 GHz), the problem is the antenna phased-array calibration. These calibration problems can be overcome, however, as the Nimbus SMMR and ESMR instruments proved. A spaceborne large-antenna radiometer still remains a challenge, however.

The sensitivity of a radiometer is a measure of its ability to detect changes in brightness temperatures of the atmosphere, terrain, or sea. A radiometer becomes less sensitive as the system temperature increases, which it does as the frequency goes up. A well-designed radiometer may have a system temperature ranging from 20 to 200 K at *L*-band, depending on whether cryogenic cooling is used or not; at *X*-band, the range is typically from 70 to 300 K, etc., [72]. Current technology using an uncooled field-effect-transistor (FET) RF amplifier allows a 100 K receiver noise temperature at *L*-band; at 30 GHz, a 500 K receiver noise temperature is obtainable without cooling. Uncooled receivers are generally used for spaceborne radiometers, since the use of cryogenics is generally difficult in space, but still meet the sensitivity requirements for many of the proposed applications. As newer low-noise solid-state amplifier devices become available over the next decade or so, it is expected that uncooled radiometers will experience a factor of 2 or more improvement in sensitivity.

3) Future Imaging Radar Technology Developments: High-resolution spaceborne imaging radars produce high data rates, use a relatively large amount of prime power, and require very fast image correlators. The critical imaging radar technology developments over the next few years will be driven by the scientific and operational requirements imposed on these sensors. These requirements include 1) long-term reliability for at least three years of operation, 2) electronic beam scanning for variable illumination geometry and wider accessible swath, 3) multipolarization simultaneous imaging, 4) multispectral capability ranging from 500 MHz up to 90 GHz, and 5) the ability to handle, transmit, and record the vast amount of data usually generated by high-resolution multiparameter sensors.

Current advances in solid-state amplifiers will allow their use as the power sources for SAR systems operating in the *L*- to *X*-band regions and possibly at higher frequencies by the early 1990s. One of the most elegant schemes for high-power radiation is the use of a distributed approach (see Fig. 28) where the amplifying elements are distributed across the aperture and colocated with the radiating elements. This scheme has numerous advantages: 1) it uses a very large number (hundreds) of amplifiers, each generating only lower power, thus allowing the use of solid-state technology, 2) it eliminates the need for combiners and high-power cables which usually result in large losses and reduce sensor efficiency, 3) it is inherently redundant and even a failure of many elements would only slightly reduce system performance, and 4) it is easily amenable to the use of phase shifters for electronic beam steering and distortion compensation.

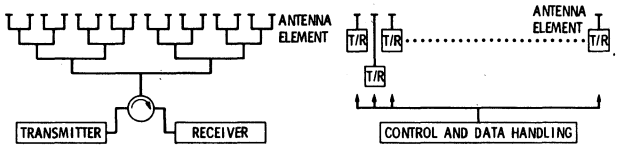

Fig. 28. Sketch illustrating the basic difference between conventional radar configuration (a) and distributed radar configuration (b).

A distributed airborne SAR sensor has recently been developed by the Jet Propulsion Laboratories and Ball Aerospace Systems Division (see Fig. 29) and is presently undergoing tests. The Shuttle Imaging Radar-C (SIR-C) is presently under development with a fully distributed, dual-frequency multipolarization capability.

An electronic scanning capability for a SAR allows the illumination of the earth's surface at a variety of angles. With the appropriate orbit drift configuration this would permit the acquisition of stereo imagery. In addition, it expands the allowable swath by being able to spontaneously control the illuminated area over a wide spatial range. This is particularly important for the observation of dynamic phenomena such as hurricanes, weather fronts, ice matrix, etc.

The simultaneous acquisition of full multipolarization data sets allows the generation of all the Stokes parameters of the polarization matrix on a pixel-by-pixel basis. In order to acquire all the polarization states (HH, VV, HV, and VH in the linear case) the antenna must be able to handle both H and V polarization vectors and the transmitter should be coupled to the H channel, then the V channel on successive pulses (or bursts of pulses). In order to keep the spaceborne sensor to a minimum size, the dual-polarization antenna capability should be achieved by dual path excitation of the same radiation elements instead of using two separate apertures.

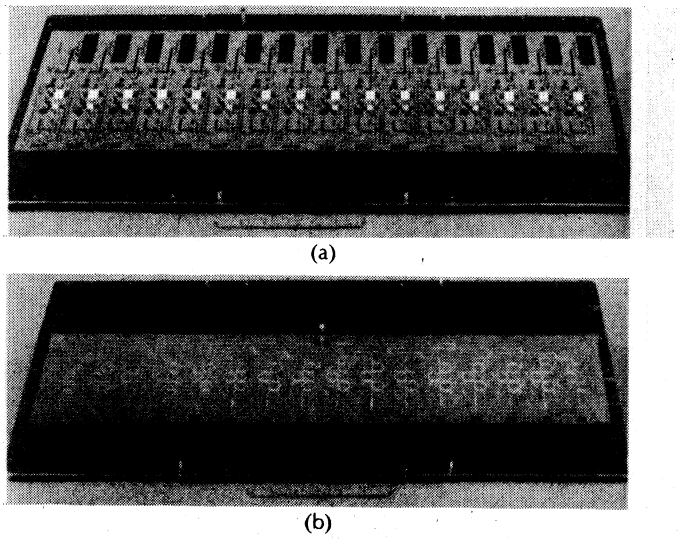

Fig. 29. Photo of a 16-element distributed airborne SAR operating at *C*-band. (a) Front side showing the radiating elements, the transmitter channels, and receiver channels. (b) Back side showing the phase shifters.

The near-simultaneous acquisition of the multipolarization data would allow easy registration of the imagery and the derivation of the relative phase on a pixel-by-pixel basis. This has been demonstrated with an airborne system (see Fig. 30).

In order to fully characterize the microwave properties of the surface and near subsurface, sensing over a wide range of the spectrum is necessary because the interaction mechanisms are strongly dependent on the electromagnetic wavelength. At long wavelengths (many tens of centimeters), the wave would probe below the surface to a depth of a few meters in dry soil or tenuous vegetation cover. At short wavelengths (a few centimeters) the wave will interact mostly with the air–surface (or surface cover) interface.

The range of the spectral region being considered for spaceborne SARs is from 500 MHz to 90 GHz. Of course, not all of this spectrum is usable because of the atmospheric opacity near 20 and 60 GHz caused, respectively, by water vapor and oxygen absorption. The low end of the region is limited principally by frequency-allocation regulations and by ionospheric effects. The upper region is limited essentially by technological factors such as the generation of high power and by atmospheric opacity.

A typical orbiting SAR sensor would require a peak radiated power in the range of 1–10 kW. This is presently technologically feasible at *L*- and *C*-bands using solid-state distributed elements. With each element having a radiated power of about 10–40 W, approximately 200–300 elements would provide the needed power. This is the basis for the SIR-C sensor under development for a 1988/89 shuttle flight. For higher frequencies, e.g., *X*-band to 40 GHz, current technology allows a maximum of a few watts of power per element. Therefore, a few thousand solid-state elements would be required to achieve the necessary power.

Future orbiting radar systems would generate data at the

• HH AMPLITUDE

• HH/VV PHASE DIFFERENCE = COLOR
• HH AMPLITUDE = BRIGHTNESS

• HH AMPLITUDE = RED
• VV AMPLITUDE = GREEN
• HV AMPLITUDE = BLUE

THE ADDITION OF PHASE INFORMATION ENHANCES THE DISCRIMINATION AND CLASSIFICATION CAPABILITY OF RADAR SENSORS

Fig. 30. Radar image of Coso Hills, CA, showing the phase difference between the direct and cross-polarized data on a pixel-by-pixel basis. At upper left is the HH image. Upper right is a false image of the amplitudes of the different polarization channels. At lower left is an image showing the phase difference between the two direct polarization channels. Data were acquired with the JPL *L*-band airborne radar (courtesy of D. Held and C. Werner, JPL).

rate of 100–300 Mbits/s. The SIR-B sensor had a data rate of 50 Mbits/s, and the SIR-C sensor will have at least a 150-Mbit/s data rate. The EOS SAR (see next section) will require a 300-Mbit/s rate. This requires the development of extremely fast data handling systems and data transmission links. On-board selective processing would be required for future operational systems. In addition, very high density storage media will be needed. For instance, the EOS SAR could generate up to 2.5×10^{13} bits per day of operation. This is the equivalent of about 250 000 computer compatible tapes (CCT) per day.

B. Future Missions and Sensors

The next decade will be a very active transition period between the early stage of experimentation with spaceborne microwave sensors and the routine application of data from these sensors for geoscientific research. This decade will be an exciting period which will see major technological advances combined with the development of new observation techniques and scientific capabilities.

1) Platforms: Advances in microwave remote sensing from space depend crucially on the availability of suitable observation platforms, and thus are inexorably tied to the relatively high cost of putting satellites—both manned and unmanned—in space. Most microwave remote sensing applications require a polar-orbiting platform with a long lifetime to optimally satisfy their needs, as demonstrated through the Nimbus series, Seasat, etc. However, these free-flyers have become increasingly expensive (approximately $300 M) so that very few new free-flyer missions have been undertaken in recent years. The Shuttle platform is currently being used for instrument technique development (e.g., the SIR series) over typically one-week missions and at a cost ranging typically from $10 M–$30 M per instrument. These missions have helped to understand optimal instrument parameters and may be viewed as an evolutionary step toward defining what sensors and sensor techniques are required for longer term polar-orbiting satellites used to study the earth as a system. The Space Station being planned by NASA includes in its concept an Earth Observation Satellite (EOS) component, which would consist of at least two polar-orbiting satellites carrying various instrument clusters including both radars and radiometers. The first of these satellites would be launched early in the next decade.

2) Future Radiometer Missions: The next generation of NOAA low-earth-orbit weather satellites due to become operational in the early 1990s would include an Advanced Microwave Sounder Unit (AMSU), a multichannel passive microwave imager with 20 imaging channels between 23 and 183 GHz, all of which would provide full earth coverage and a spatial resolution of about 15 km. This would be used for both water vapor and temperature sounding on an image basis. Also in the planning stage is the Upper Atmospheric Research Satellite (UARS) which includes a microwave limb scanner to observe O_3, H_2O_2, ClO, H_2O, etc., emissions in the stratosphere, mesosphere, and lower thermosphere, providing a fairly high-resolution view of many tens of atmospheric molecular species. This will lead to global measurements in the upper atmosphere of the abundances of these molecular species and, along with the measurement of winds, magnetic field, temperature, etc., will improve our understanding of the upper atmospheric transport and chemical processes. Limb-sounders provide improved sensitivities and resolution over nadir-viewing instruments.

Other microwave radiometer experiments are being

Mission	Seasat	SIR-A	SIR-B	SIR-C	SIR-D	EOS
Launch date	1978	1981	1984	1988/9	1991	1993/4
Altitude (km)	800	240	220	250	250	700
Frequency (band)	*L*	*L*	*L*	*L/C*	*L/C/X/K*	*L/C/X/K*
Resolution (m)	25	40	20	20	20	20
Swath width (km)	100	50	50	50	50	100–200
Incidence angle (deg)	20	48	15–60	15–60	15–60	15–60
Polarization	HH	HH	HH	HH/VV/HV	HH/VV/HV	HH/VV/HV
Type (*)	C	C	C	D	D	D
Scanning (**)			M	E	E	E

*Types: C = conventional SAR, D = distributed SAR.
**Scanning: M = mechanical, E = electronic.

planned as part of the Shuttle program as well as dedicated earth observation free-flyers such as ESA's ERS-1 (discussed below).

3) Future Radar Missions:

a) Shuttle and Space Station missions: The Shuttle Imaging Radar (SIR) series, with two successful missions already completed (SIR-A and SIR-B), will continue to form the core of the U.S. program over the next several years for the development of the full capability of active microwave imagers (Table 3). The next such mission, SIR-C, is planned for a 1988 launch and will have the capability of imaging the earth's surface using all polarization states (HH, VV, and HV) and using at least two frequencies (*L*- and *C*-band). This sensor will most likely be flown using a third band by using a German-developed *X*-band imaging radar, thereby allowing three-frequency imaging. This would be the true equivalent of a "color" radar. This will be followed by a 1990 SIR-D mission using a four-frequency capability (*L*-, *C*-, *X*-, and *K*-bands). Both SIR-C and SIR-D will use electronic beam scanning and will be calibrated. Both will be used to conduct a variety of geoscientific investigations and to develop the technology necessary for a long-duration orbiting SAR on the Earth Observation Satellite (EOS) scheduled for launch in the early 1990s.

b) ESA, Japanese, Canadian free-flyers: In the same period, a number of other free-flying SAR systems will be in orbit on ESA, Japanese, and Canadian satellites. These SAR missions are being developed for very specific scientific or operational objectives and have limited flexibility for multiparameter earth observations. For example, the ESA Resources Satellite-1 (ERS-1) is scheduled to include a *C*-band SAR with 30-m resolution and 100-km swath; it will focus mainly on long-term oceanic observations. ERS-1 will also include a six-frequency imaging microwave radiometer (IMR), a dual-frequency scatterometer for oceanic wind direction and velocity, and a radar altimeter for sea state observations. The National Space Agency of Japan (NASDA) is planning a Japanese Earth Resources Satellite (ERS-1) which would carry an *L*-band SAR with 25-m resolution and 75-km swath; the launch date would be in the 1987–1988 period. The Japanese ERS-1 (not to be confused with the ESA ERS-1) would focus mainly on geological mapping, primarily surface feature morphology. The Canadian Radarsat, scheduled for a 1990 launch, would carry a *C*-band SAR primarily for the purpose of monitoring polar ice dynamics for use in ship routing; it would have a swathwidth of approximately 200 km.

c) Planetary exploration: In the planetary exploration areas, imaging radars are the key elements for exploration of two solar system bodies which are continuously and completely cloud-covered, Venus and Titan. In the case of Venus, a radar sensor on the Pioneer Venus Orbiter (PVO) provided low-resolution (40–100-km) images in the late 1970s. More recently, a Russian Venera mission acquired radar images of part of the northern hemisphere at a resolution of a few kilometers. A much more sophisticated sensor will be put in orbit around Venus in 1988 as part of the U.S. Venus Radar Mission (VRM) with the objective of providing global coverage at a resolution of about 150 m.

In the case of Titan, a satellite of Saturn, the larger distance to earth will put a very tight limit on the data rate transmission which directly impacts the mapping coverage and resolution. In this case, spacecraft will be put in orbit around Saturn and, on selective orbits, will fly by Titan. These flybys will be targeted in such a way that during each one of them a different region of the satellite is mapped. Preliminary mission scenarios allow about 20 flybys. Because of the very strong desire for global mapping, the Titan Radar Mapper will have a very wide swath (600–800 km) low-resolution (6–40-km) capability using real-aperture imaging techniques. Over limited regions, a synthetic-aperture mode will be used to acquire high-resolution (about 200-m) snapshots. The Titan Radar Mapper is planned as part of the Cassini mission, scheduled for launch in the mid-1990s.

d) Ocean scatterometry: In the field of ocean scatterometry, two quasi-operational systems will be put in orbit in the early 1990s. A NASA *K*-band scatterometer (NSCAT) will be part of the Navy Remote Ocean Sensing System (NROSS), a polar orbiter at 830-km altitude which will also include a radar altimeter, a special sensor microwave/imager (SSM/I), and a low-frequency microwave radiometer. The primary purpose of NSCAT, which uses the Seasat scatterometer heritage, is to obtain accurate measurements of global oceanic winds for oceanography and meteorology. NSCAT is expected to provide accurate wind measurements over at least 90 percent of the global, ice-free ocean with a sampling frequency of at least every two days over a three-year period. It is expected to obtain wind speed accuracies of about 2 m/s for wind speeds from 3 to 30 m/s, and to be useful for wind measurements up to 100 m/s [73]. The NSCAT instrument will use six fan-beam antennas and will result in reduced wind directional ambiguities in comparison to the Seasat SASS which used only four beams. The second scatterometer system is a dual-frequency *C*-band instrument as part of the ERS-1 payload.

Table 4 Characteristics of the Seasat SASS, NROSS, and ERS-1 Scatterometers

	Seasat SASS	NROSS NSCAT	ERS-1 SCATT
Launch date	1978	1990	1988
Altitude (km)	800	830	775
Orbit inclination (deg)	108	98.7	98.5
Frequency (GHz)	14.599	13.995	5.3
Polarization	dual	dual	HH
Swath (km)	750	600	500
Sample size (km)	50	25	50
Antennas	4	6	3

Both systems have similar capabilities (see Table 4) which will allow global mapping of the surface wind field every three days. More advanced systems are planned for EOS use in the mid-1990s.

e) Altimetry: The next major radar altimetry project being planned by the U.S. is TOPEX (Ocean Topography Experiment), scheduled for a 1990 launch. The objective of the TOPEX mission is to acquire global ocean surface topographic information for the study of ocean circulation and tidal changes. TOPEX would be placed in a 1300-km altitude orbit with 65° inclination, and its orbital altitude would be determined to an accuracy of 5 cm by using special radio and laser tracking systems. The altimeter would operate at two frequencies, which provides a means for correcting ionospheric interference errors. TOPEX would also include a microwave radiometer for correcting interference in the altimetric data due to atmospheric water vapor. TOPEX is planned for a 3–5-year minimum lifetime.

In the case of solid-surface altimetry, global high-resolution topographic mapping will be accomplished on Mars before it is done on our own planet. A 37-GHz altimeter on the Mars Orbiter Mission (1990 launch) will allow complete topographic mapping of the planet with about 15-m-height resolution and 2-km footprints. This will be sufficient for geophysical studies and local morphological studies. In the case of the earth's surface, a Shuttle Scanning Radar Altimeter (Fig. 31) will use an electronically scanned 37-GHz synthetic-aperture altimeter to acquire global land topography with a height resolution of a few meters and footprints of a few hundred meters. This system is under study for an early 1990s launch.

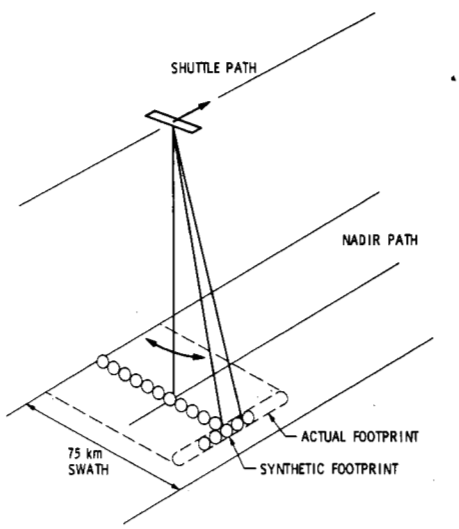

Fig. 31. Conceptual sketch of a spaceborne scanning radar altimeter. The surface footprint corresponds to the real-aperture resolution across track and synthetic-aperture resolution along track. Wide coverage will be achieved by electronic scanning. Altitude resolution is defined by the pulse length.

V. Conclusions

Microwave remote sensing offers unique information for geoscientific studies of the earth and planets. Both radars and radiometers have been developed and flown on a variety of satellites and have shown the potential and value for these sensors for information such as land-surface morphology and sea-surface topography, soil moisture, ice dynamics and type, oceanic winds and waves, vegetation characteristics, atmospheric water vapor, and atmospheric temperature profiles, to name just a few. These microwave perspectives of the earth are synergistic with those obtained in other portions of the spectrum and will be further exploited in future satellite systems.

References

[1] J. McCauley *et al.*, "Subsurface valleys and geoarcheology of the eastern Sahara revealed by Shuttle Roder," *Science*, vol. 218, p. 1004, 1982.

[2] A. R. Hibbs and W. S. Wilson, "Satellites map the oceans," *IEEE Spectrum*, vol. 20, pp. 46–53, Oct. 1983.

[3] E. G. Njoku, "Passive microwave remote sensing of the earth from space—A review," *Proc. IEEE*, vol. 70, no. 7, pp. 728–750, July 1982.

[4] R. L. Cosgriff, W. H. Peake, and R. C. Taylor, "Terrain scattering properties for sensor system design (terrain handbook II)," in *Engr. Exp. Stn. Bull.*, no. 181, p. 29, Ohio State Univ., 1960.

[5] W. H. Peake, "Interaction of electromagnetic waves with some natural surfaces," *IRE Trans. Antennas Propagat.*, vol. AP-7, pp. 5324–329, 1959.

[6] A. Viksne, T. C. Liston, and C. D. Sapp, "SLR reconnaissance of Panama," *Geophys.*, vol. 34, pp. 54–64, 1969.

[7] H. C. MacDonald, "Geologic evaluation of radar imagery from Darien Province, Panama," *Modern Geology*, vol. 1, pp. 1–63, 1969.

[8] R. K. Moore, J. P. Claassen, A. C. Cook, D. L. Fayman, J. C. Holtzman, A. Sobti, W. E. Spencer, F. T. Ulaby, J. D. Young, W. J. Pierson, V. J. Cardone, J. Hayes, W. Spring, R. J. Kern, and N. M. Hatcher, "Simultaneous active and passive microwave responses of the earth—The Skylab Radscat experiments," in *Proc. 9th Int. Symp. on Remote Sensing Environment* (Ann Arbor, MI, 1974), p. 189.

[9] R. L. Jordan, "The Seasat—A synthetic aperture radar system;" *IEEE J. Oceanic Eng.*, vol. OE-5, pp. 154–163, 1980.

[10] J. P. Claassen, R. K. Moore, H. S. Fung, and W. J. Pierson, Jr., "Radar sea return and the Radscat satellite anemometer," in *IEEE Conf. Rec. Oceans '72* (IEEE Publ. 72 CHO 660-1 OCC), 1972, pp. 180–185.

[11] F. T. Barath, A. H. Barrett, J. Copeland, D. E. Jones, and A. E. Lilley, "Mariner 2 microwave radiometer experiment and results," *Astron. J.*, vol. 69, no. 1, 1964.

[12] A. E. Basharinov, A. S. Gurvich, S. T. Yegorov, A. A. Kurskaya, D. T. Matveyev, and A. M. Shutko, "The results of microwave sounding of the earth's surface according to experimental data from the satellite Cosmos 243," in *Space Research XI*. Berlin: Akademie-Verlag, 1971.

[13] D. H. Staelin, A. L. Cassel, K. F. Kunzi, R. L. Pettyjohn, R. K. L. Poon, P. W. Rosenkranz, and J. W. Waters," Microwave atmospheric temperature sounding: effects of clouds on the Nimbus-5 satellite data," *J. Atm. Sci.*, vol. 32, p. 1970, 1975.

[14] L. J. Ippolito, "Radio propagation for space communication systems," *Proc. IEEE*, vol. 69, no. 6, 697–727, June 1981.

[15] F. T. Ulaby and K. R. Carver, "Passive microwave remote sensing," *Manual of Remote Sensing*, vol. 1. Falls Church, VA.: American Soc. of Photogrammetry, 1983, ch. 11, pp.

475–516.
[16] F. T. Ulaby, R. K. Moore, and A. K. Fung, *Microwave Remote Sensing*, vol. 1. Reading, MA: Addison-Wesley, 1981.
[17] ———, *Microwave Remote Sensing*, vol. 2, Reading, MA: Addison-Wesley, 1982.
[18] ———, *Microwave Remote Sensing*, vol. 3. Dedham, MA: Artech House, 1985.
[19] D. H. Staelin, "Passive remote sensing at microwave wavelengths," *Proc. IEEE*, vol. 57, no. 4, pp. 427–439, Apr. 1969.
[20] L. A. Klein and C. T. Swift, "An improved model for the dielectric constant of sea water at microwave frequencies," *IEEE Trans. Antennas Propagat.*, vol. AP-25, p. 104, 1977.
[21] J. P. Hollinger, "Passive microwave measurements of sea surface roughness," *IEEE Trans. Geosci. Electron.*, vol. GE-9, p. 165, 1971.
[22] T. T. Wilheit, "A review of applications of microwave radiometry to oceanography," *Boundary-Layer Meterol.*, vol. 13, pp. 277–293, 1978.
[23] ———, "A model for microwave emissivity of the ocean's surface as a function of wind speed," *IEEE Trans. Geosci. Electron.*, vol. GE-17, pp. 244–249, 1979.
[24] W. Nordberg, J. Conaway, D. B. Ross, and T. Wilheit, "Measurements of microwave emission from a foam-covered, wind-driven sea," *J. Atmos. Sci.*, vol. 28, p. 429, 1971.
[25] T. T. Wilheit, J. Blinn, W. Campbell, A. Edgerton, and W. Nordberg, "Aircraft measurements of microwave emission from Arctic sea ice," in *NASA Goddard Space Flight Center Tech. Rep.* X651-71-417, 1971.
[26] B. E. Troy, J. P. Hollinger, R. M. Lerner, and M. M. Wisler, "Measurement of the microwave properties of sea ice at 90 GHz and lower frequencies," *J. Geophys. Res.*, vol. 86, pp. 4283–4289, 1981.
[27] H. J. Zwally and P. Gloersen, "Passive microwave images of the polar regions and research applications," *Polar Rec.*, vol. 18, no. 116, 1976.
[28] F. D. Carsey, "Arctic sea ice distribution at end of summer 1973–1976 from satellite microwave data," *J. Geophys. Res.*, vol. 87, pp. 5809–5835, 1982.
[29] D. J. Cavalieri, S. Martin, and P. Gloersen, "Nimbus 7 SMMR observations of the Bering Sea ice cover during March 1979," *J. Geophys. Res.*, vol. 88, pp. 2743–2754, 1983.
[30] J. C. Comiso, "Sea ice effective microwave emissivities from satellite passive microwave and infrared observations," *J. Geophys. Res.*, vol. 88, pp. 7686–7704, 1983.
[31] J. C. Comiso, S. F. Ackley, and A. L. Gordon, "Antarctic sea ice microwave signatures and their correlation with *in-situ* ice observations," *J. Geophys. Res.*, vol. 89, pp. 662–672, 1984.
[32] T. J. Schmugge, "Remote sensing of soil moisture: Recent advances," *IEEE Trans. Geosci. Remote Sensing*, vol. GE-21, no. 3, pp. 336–344, July 1983.
[33] R. W. Newton and J. W. Rouse, "Microwave radiometer measurements of moisture content," *IEEE Trans. Antennas Propagat.*, vol. AP-28, pp. 680–686, 1980.
[34] K. P. Kirdiashev, A. A. Chukhlantsev, and A. M. Shutko, "Microwave radiation of the earth's surface in the presence of vegetation cover" (translation), *Radiotekh. i Elektron.*, vol. 24, pp. 256–264, 1979.
[35] J. R. Wang, "The dielectric properties of soil-water mixtures at microwave frequencies," *Radio Sci.*, vol. 15, pp. 977–985, 1980.
[36] F. T. Ulaby and W. H. Stiles, "The active and passive microwave response to snow parameters, Part II: Water equivalent of dry snow," *J. Geophys. Res.*, vol. 85, pp. 1045–1049, 1980.
[37] W. H. Stiles and F. T. Ulaby, "The active and passive microwave response to snow parameters, Part I: Wetness," *J. Geophys. Res.*, vol. 85, pp. 1037–1044, 1980.
[38] R. Hofer and C. Matzler, "Investigations on snow parameters by radiometry in the 3- to 60-mm wavelength region," *J. Geophys. Res.*, vol. 85, pp. 453–460, 1980.
[39] F. T. Ulaby, "Radar signatures of terrain: Useful monitors of renewable resources," *Proc. IEEE*, vol. 70, no. 12, pp. 1410–1428, Dec. 1982.
[40] G. Pettengill *et al.*, "Pioneer Venus radar results: Altimetry and surface properties," *J. Geophys. Res.*, vol. 85, p. 8261, 1980.
[41] R. S. Saunders, "Questions for the geologic exploration of Venus," *J. British Interplanetary Soc.*, vol. 37, p. 435, 1984.
[42] R. B. Chadwick and E. E. Gossard, "Radar remote sensing of the clear atmosphere—Review and applications," *Proc. IEEE*, vol. 71, no. 6, pp. 738–753, June 1983.
[43] D. H. Staelin, "Passive microwave remote sensing of the atmosphere from satellites," in *Proc. Int. Geosc. Remote Sensing Symp.*, vol. 1, pp. 413–416, ESA SP-215, 1984.
[44] ———, "Passive microwave techniques for geophysical sensing of the earth from satellites," *IEEE Trans. Antennas Propagat.*, vol. AP-29, pp. 683–687, 1981.
[45] F. F. Sabins, R. Blom, and C. Elachi, "Seasat radar image of the San Andreas fault, California," *Amer. Assoc. Petrol. Geol.*, vol. 64, p. 614, 1980.
[46] R. G. Blom and C. Elachi, "Spaceborne and airborne imaging radar observations of sand dunes," *J. Geophys. Res.*, vol. 86, p. 3061, 1981.
[47] F. F. Sabins, "Geologic interpretation of space shuttle radar images of Indonesia," *Amer. Assoc. Petr. Geol. Bull.*, vol. 67, pp. 2076–2099, 1983.
[48] C. Elachi *et al.*, "Shuttle Imaging Radar experiment," *Science*, vol. 218, p. 996, 1982.
[49] R. G. Blom, R. J. Crippen, and C. Elachi, "Detection of subsurface features in Seasat radar images of Means Valley, Mojave Desert, California," *Geology*, vol. 12, p. 346, 1983.
[50] J. Ford, "Geological mapping from spaceborne imaging radars: Kentucky–Virginia, USA," in *Digest IEEE 1982 Int. Geoscience and Remote Sensing Symp.* (Munich, Germany), p. FA6, 1982.
[51] G. Wadge and T. H. Dixon, "A geological interpretation of Seasat SAR imagery of Jamaica," *J. Geology*, vol. 92, p. 561, 1984.
[52] C. Elachi, L. Roth, and G. Schaber, "Spaceborne radar subsurface imaging in hyperarid regions," *IEEE Trans. Geosci. Remote Sensing*, vol. GE-22, p. 383, 1984 (Note: In this article, the SIR-A and Landsat images in Fig. 2 were mistakenly interchanged.)
[53] C. Elachi and N. Engheta, "Radar scattering from a diffuse vegetation layer," *IEEE Trans. Geosci. Remote Sensing*, vol. GE-20, p. 212, 1982.
[54] M. Kobrick *et al.*, "Convergent stereo with the Shuttle Imaging Radar," submitted to *Photogramm. Engr. Remote Sensing*, 1984.
[55] F. T. Ulaby and W. H. Stiles, "Microwave response of snow," *Adv. Space Res.*, vol. 1, pp. 131–149, 1981.
[56] C. Matzler and E. Schanda, "Snow mapping with active microwave sensors," *Int. J. Remote Sensing*, vol. 5, pp. 409–422, 1984.
[57] F. P. Bretherton, "Earth System Science and remote sensing," this issue, pp. 1118–1127.
[58] J. D. Erickson, A. J. Tuyahov, and H. C. Hogg, "Understanding global changes on the land: A potential focus for NASA earth sciences and land remote sensing," in *Dig. 1983 IEEE Int. Geoscience and Remote Sensing Symp.* (San Francisco, CA), IEEE Cat. No. 83CH1837-4, pp. 6.1–6.5, 1983.
[59] D. L. Peterson, D. A. Mouat, and S. Running, "Characterization of terrestrial ecosystems for biogeochemical studies using remote sensing," in *Dig. 1983 IEEE Int. Geoscience and Remote Sensing Symp.* (San Francisco, CA), IEEE Cat. No. 83CH1837-4, pp. 7.1–7.6, 1983.
[60] R. H. Waring, J. Rogers, and W. T. Swank, "Water relations and hydrologic cycles," in *Dynamic Properties of Forest Ecosystems*, D. E. Kiechle, Ed. New York: Cambridge Univ. Press, 1981, pp. 213–216.
[61] P. Hoogeboom, "Classification of agricultural crops in radar images," *IEEE Trans. Geosci. Remote Sensing*, vol. GE-21, pp. 329–336, 1983.
[62] S. T. Wu, "Analysis of data acquired by synthetic aperture radar and Landsat Multispectral Scanner over Kershaw County, South Carolina during the summer season, AgRISTARS pub. no. DC-Y2-04374; NSTL/ERL-213, Nat. Space Tech. Labs., NSTL, Stn., MS, 1983.
[63] W. J. Campbell, Ed., "Ice and climate experiment—ICEX; Report of Science and Applications Working Group," pub. by NASA Goddard Space Flight, Dec. 1979.
[64] P. G. Teleki, W. J. Campbell, R. O. Ramseier, and D. Ross, "The offshore environment: A perspective from Seasat-1 SAR data," in *Proc. 11th Ann. Offshore Tech. Conf.*, (Houston, TX), pp. 215–220, 1979.
[65] R. L. Brooks, W. J. Campbell, R. O. Ramseier, H. R. Stanley,

and H. J. Zwally, "Ice sheet topography by satellite altimetry," *Nature*, vol. 274, pp. 539–543, 1978.
[66] R. Hofer, E. G. Njoku, and J. W. Waters, "Microwave radiometric measurements of sea surface temperature from the Seasat satellite: first results," *Science*, vol. 212, p. 1385, 1981.
[67] C. T. Swift, "Passive microwave remote sensing of the ocean —A review," *Bound. Layer Meteor.*, vol. 13, pp. 277–293, 1980.
[68] H. C. Blume, B. M. Kendall, and J. C. Fedors, "Measurements of ocean temperature and salinity via microwave radiometry," *Boundary Layer Meteor.*, vol. 13, p. 295, 1978.
[69] W. F. Townsend, "An initial assessment of the performance achieved by the Seasat radar altimeter," *IEEE J. Oceanic Eng.*, vol. OE-5, pp. 80–92, 1980.
[70] L-L Fu and B. Holt, "Seasat views oceans and sea ice with synthetic aperture radar," JPL Publ. 81-120, Jet Propulsion Lab., Pasadena, CA, 1982.
[71] R. C. Beal, "Spectrasat: A concept for the collection of global directional wave spectra," in *Proc. 1984 IEEE Int. Geoscience and Remote Sensing Symp.*, vol. II (Strasbourg, France), ESA SP-215, pp. 781–786, 1984.
[72] D. H. Staelin and P. W. Rosenkranz, Eds., "High resolution passive microwave satellites: applications review panel final report," MIT Res. Lab of Electronics, Cambridge, MA, 1978.
[73] F. Li, P. Callahan, M. Freilich, D. Lame, and C. Winn, "NASA Scatterometer on NROSS—A system for global observation of oceanic winds," in *Proc. 1984 IEEE Int. Geoscience and Remote Sensing Symp.*, vol. II (Strasbourg, France), ESA SP-215, pp. 777–780, 1984.
[74] D. B. Chelton, K. J. Hussey, and M. E. Parks, "Global satellite measurements of water vapour, wind speed and wave height," *Nature*, vol. 254, p. 529, 1981.

• HH AMPLITUDE

• HH AMPLITUDE = RED
• VV AMPLITUDE = GREEN
• HV AMPLITUDE = BLUE

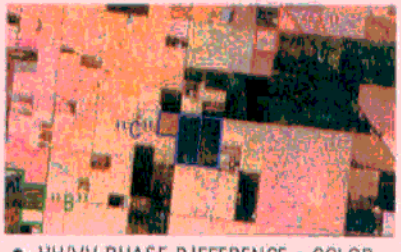

• HH/VV PHASE DIFFERENCE = COLOR
• HH AMPLITUDE = BRIGHTNESS

THE ADDITION OF PHASE INFORMATION ENHANCES THE DISCRIMINATION AND CLASSIFICATION CAPABILITY OF RADAR SENSORS

Fig. 30. Radar image of Coso Hills, CA, showing the phase difference between the direct and cross-polarized data on a pixel-by-pixel basis. At upper left is the HH image. Upper right is a false image of the amplitudes of the different polarization channels. At lower left is an image showing the phase difference between the two direct polarization channels. Data were acquired with the JPL *L*-band airborne radar (courtesy of D. Held and C. Werner, JPL).

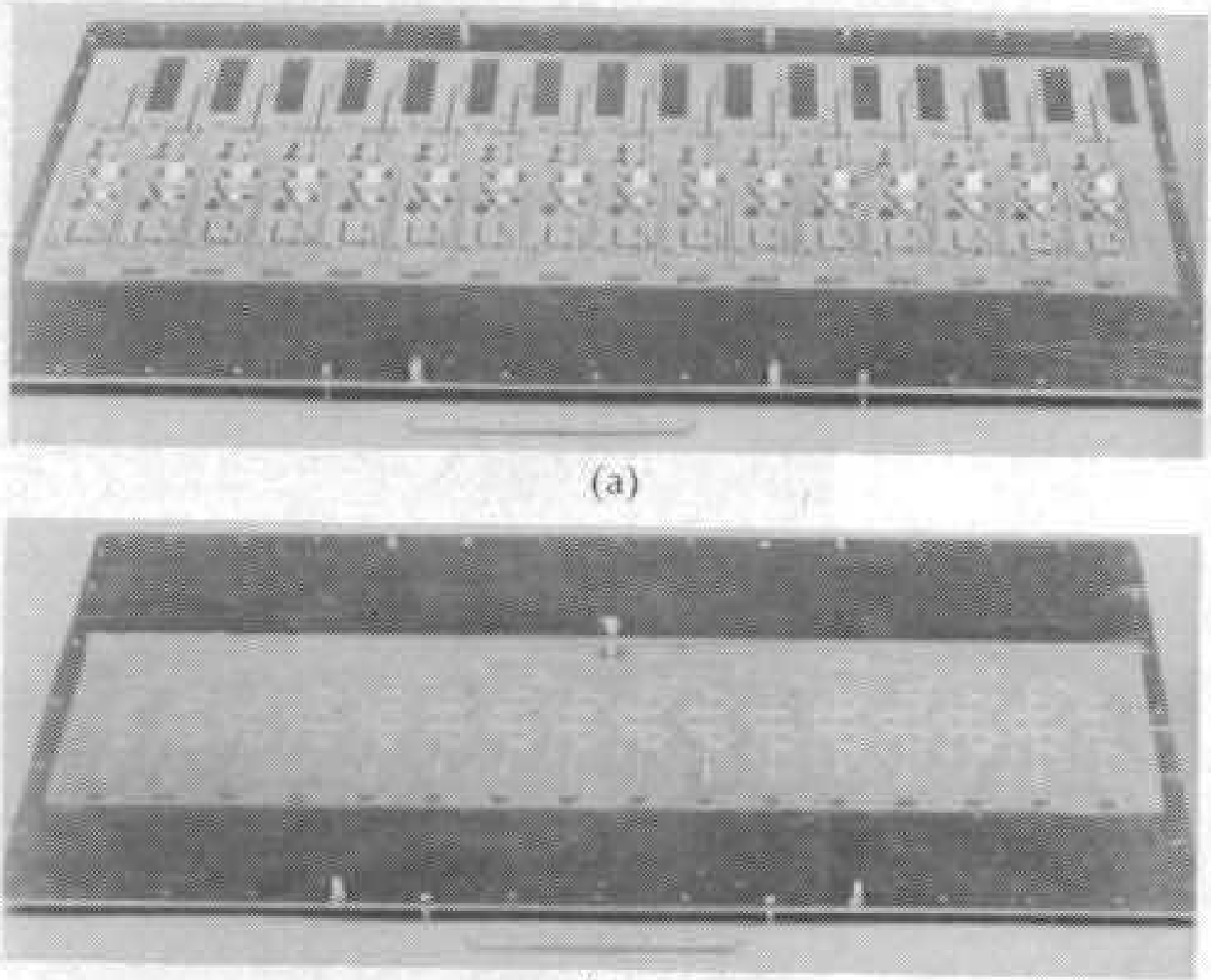

(a)

(b)

Fig. 29. Photo of a 16-element distributed airborne SAR operating at C-band. (a) Front side showing the radiating elements, the transmitter channels, and receiver channels. (b) Back side showing the phase shifters.

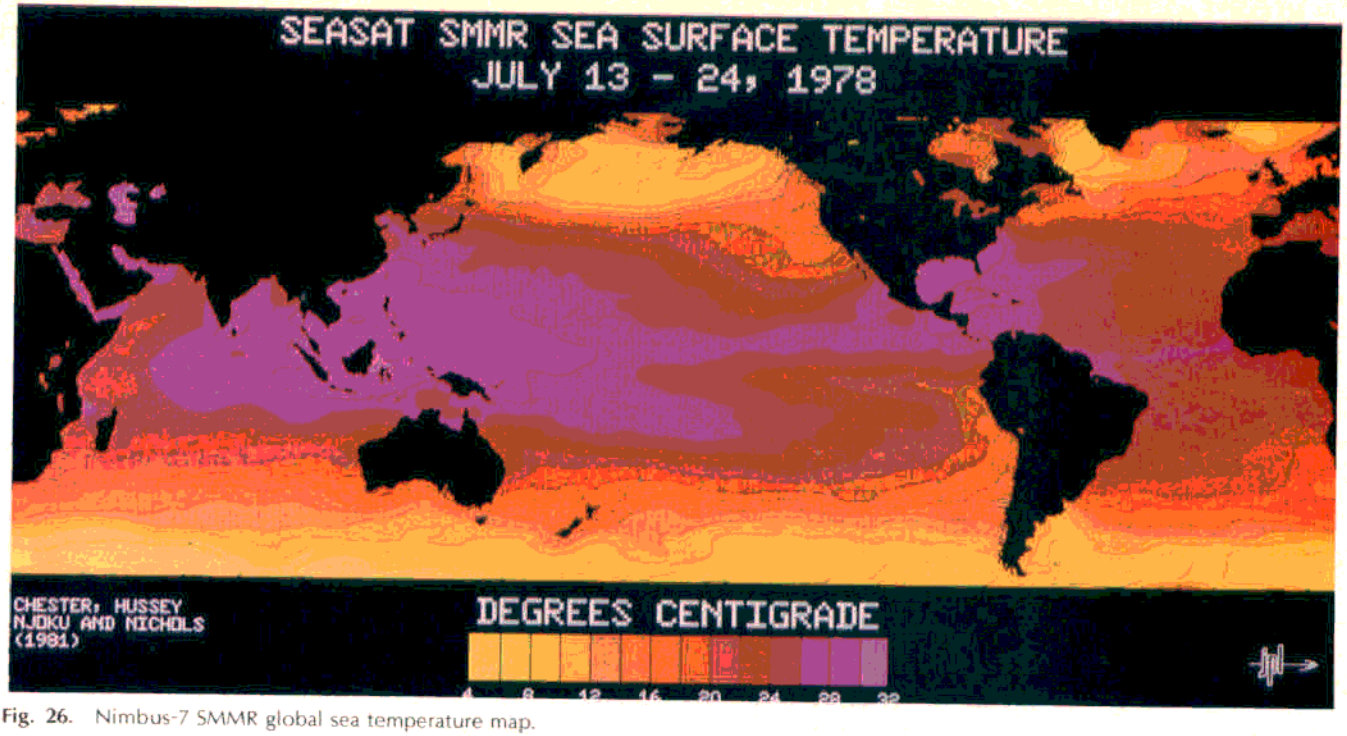

Fig. 26. Nimbus-7 SMMR global sea temperature map.

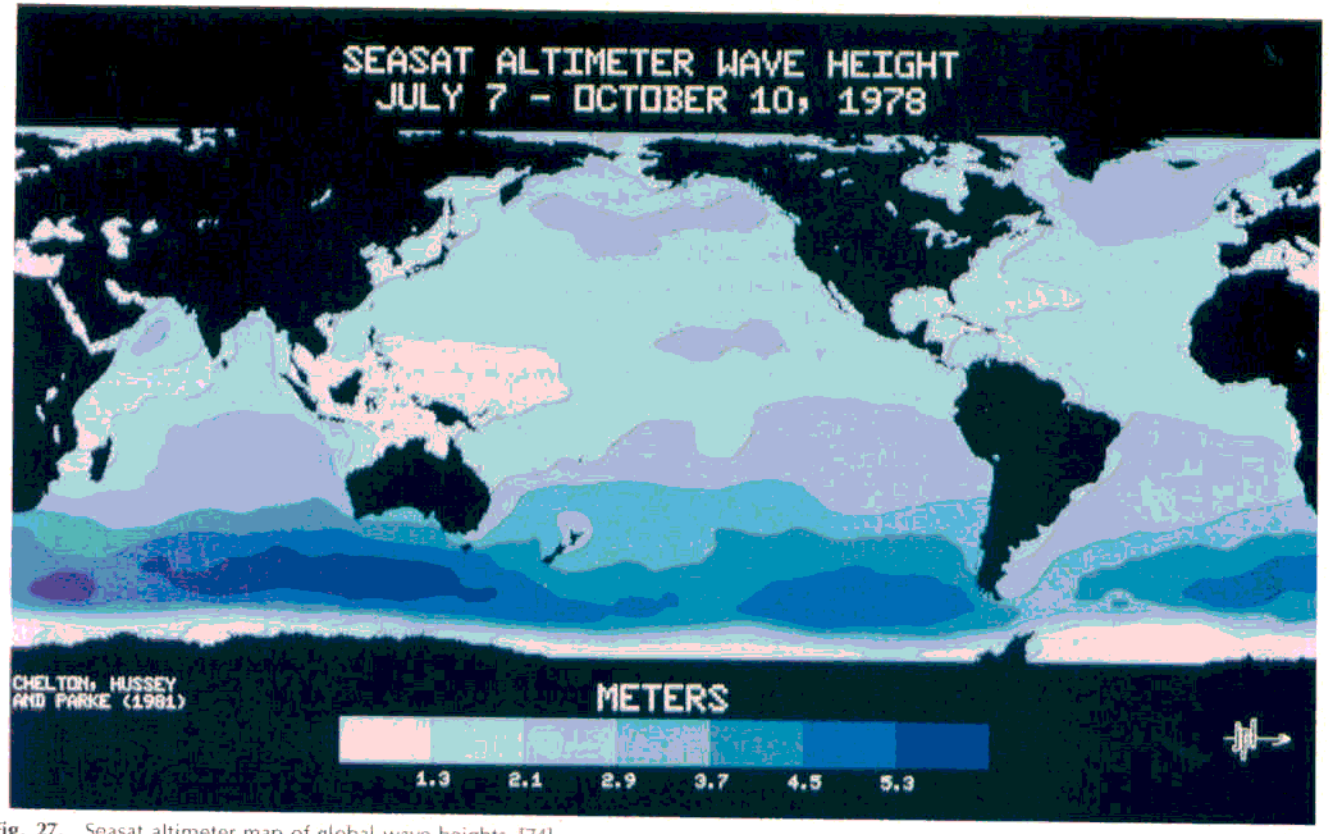

Fig. 27. Seasat altimeter map of global wave heights. [74].

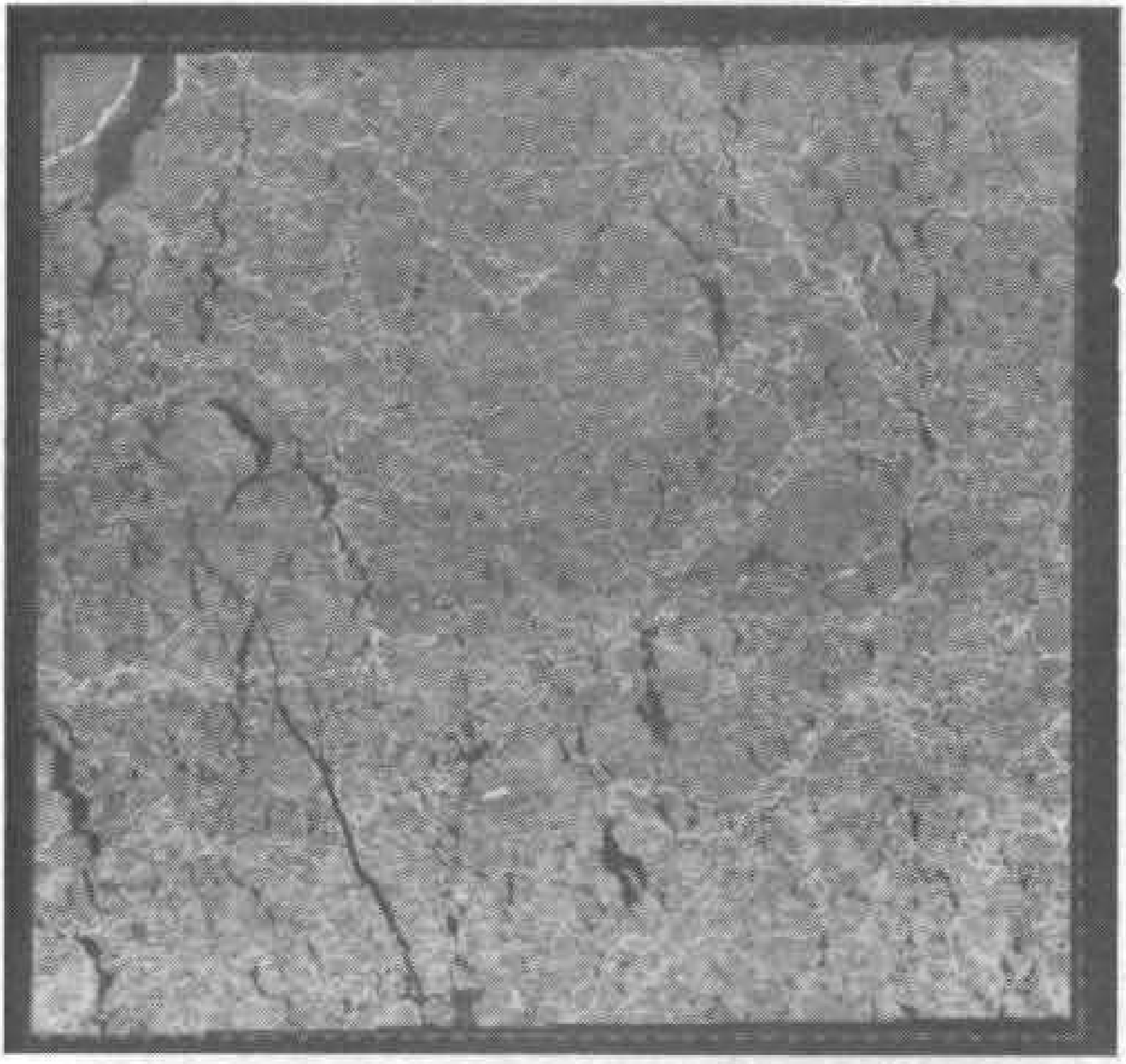

Fig. 24. Seasat SAR image of a region in Beaufort Sea, showing small ice island entrapped (at 6 o'clock, 2/3 way down from center).

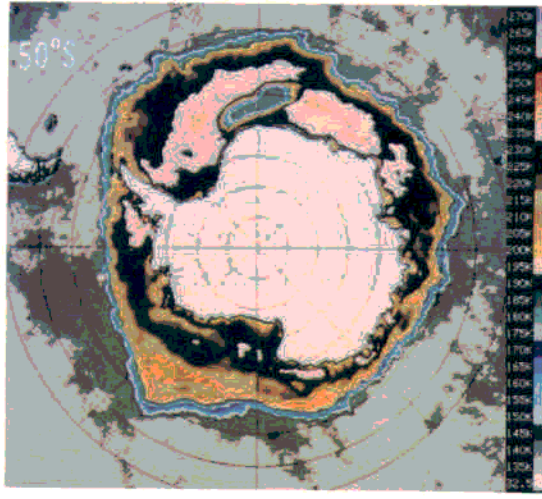

(a)

WINTER

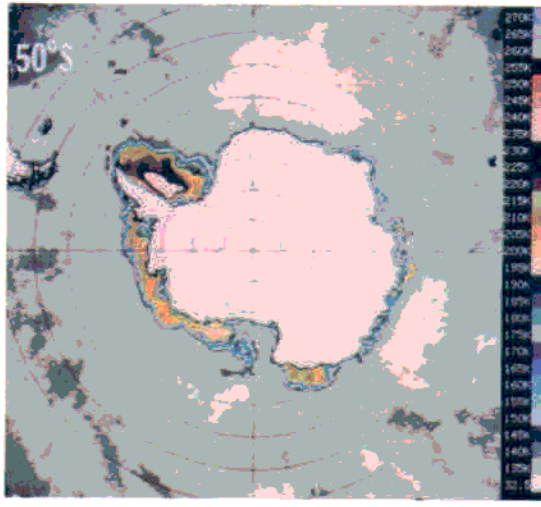

(b)

SUMMER

Fig. 23. ESMR passive microwave images of the Antarctic polar region. (a) Winter, showing extent of pack ice. (b) Summer, showing greatly contracted size of pack ice.

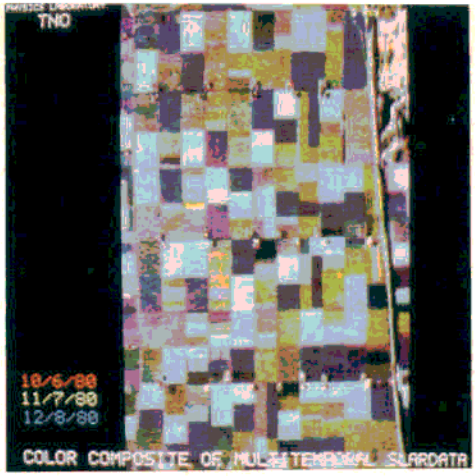

(a)

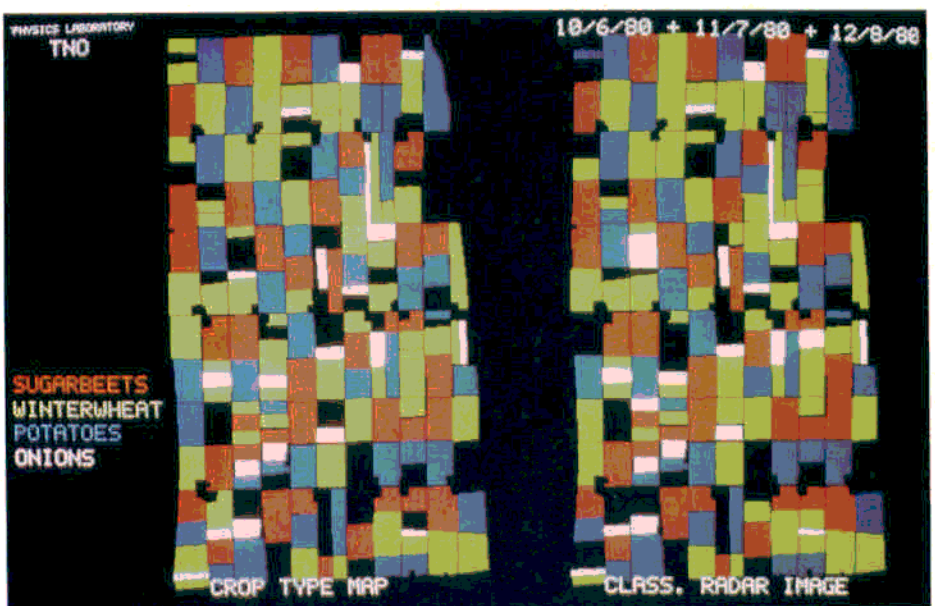

(b) (c)

Fig. 19. Crop classification with multidate observations by X-band SLAR. (a) Color composite of three SLAR images. (b) Crop type map. (c) Crop type as classified by the radar image-composite shown in (a) (images are courtesy of Hoogeboom; see Hoogeboom, [61]).

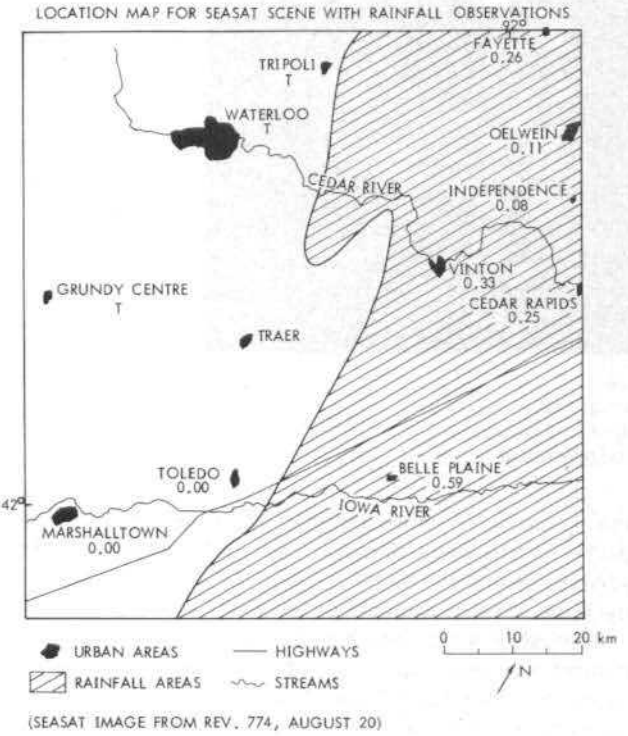

(b)

Fig. 18. Color-enhanced Seasat SAR image delineating rainfall extent over central Iowa (a) and the corresponding location maps (b) for rainfall observations. Light blue color represents areas that received significant rain on the day prior to the Seasat overpass. The green and orange colors represent areas with relatively dry soil conditions. The color coding was generated on the basis of the image intensity of the original SAR image (Ulaby *et al.*, [17]).

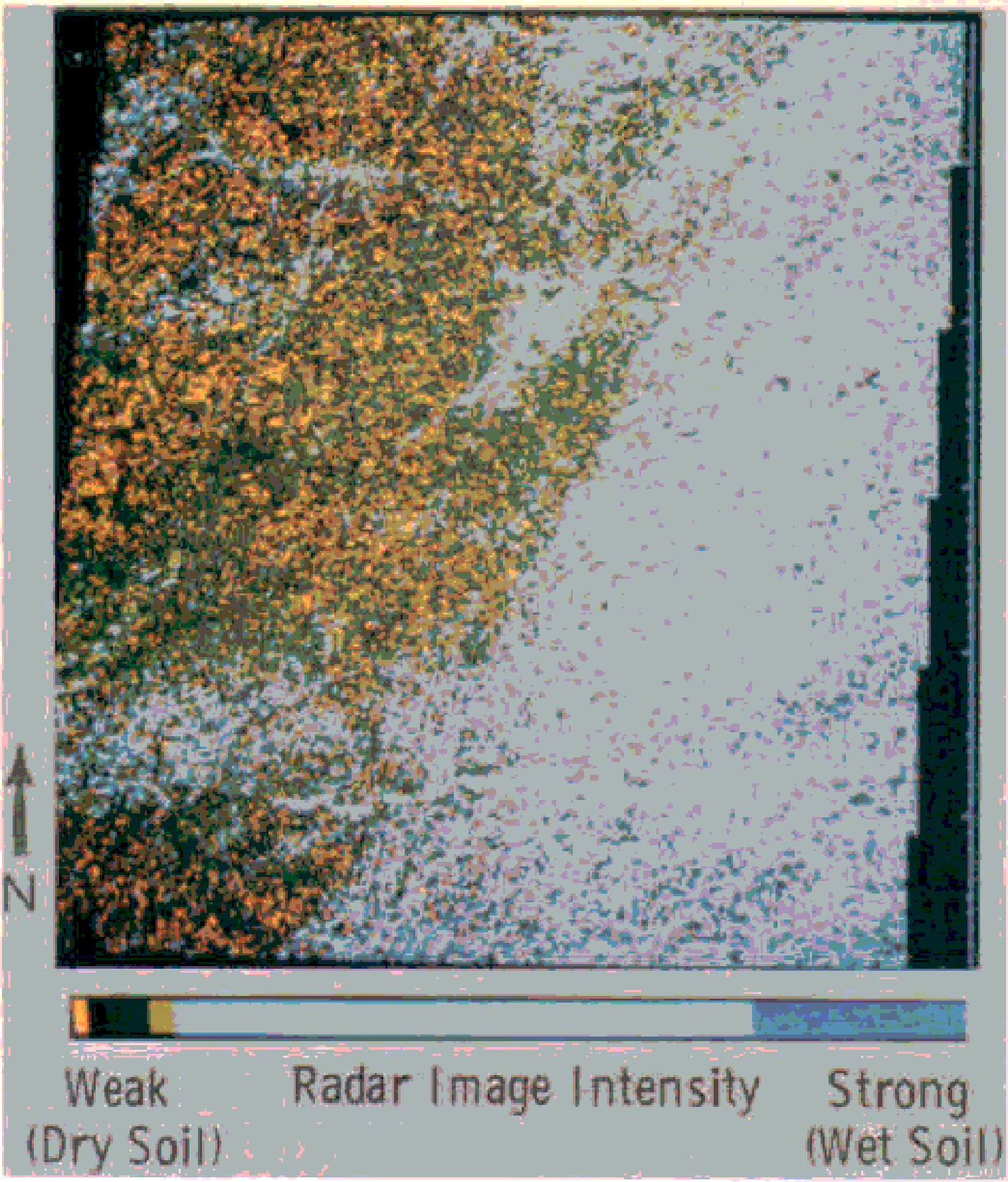

(a)

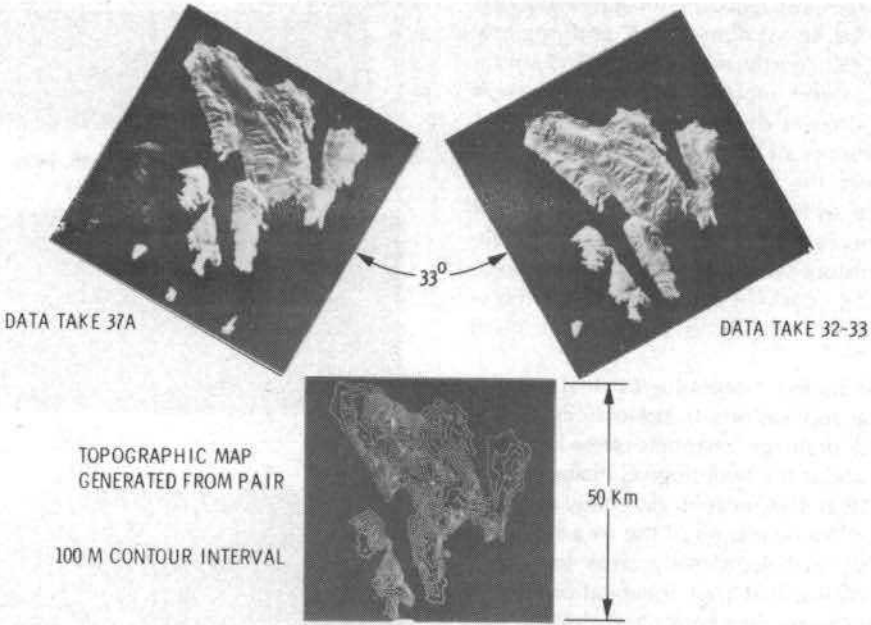

Fig. 17. Stereo pair images of the island of Cephalonia in Greece, acquired with SIR-A in 1981. The angle of convergence is only 5°. This still allows stereo observation.

(a)

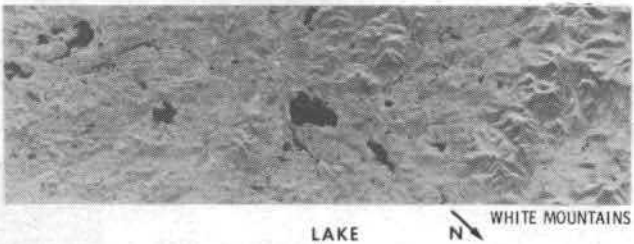

(b)

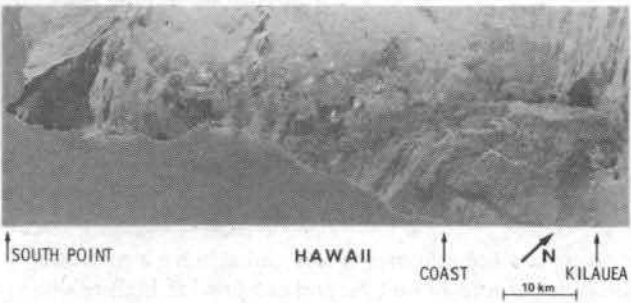

(c)

Fig. 16. Radar images of a variety of geologic surfaces acquired with SIR-B in October 1984. (a) Folded, layered rocks of the Paleocene Age (20 million years old) in the high plateau of northern Peru show extreme dissection and local offsets of the rocks due to faulting. At the center of the image is the Maranon River which is a major tributary of the Amazon. Radar incidence angle is 55°. The image is approximately 15 km × 15 km. Location is 4°54′ S and 78°20′ W. (b) Glacially sculpted terrain in New Hampshire and southwestern Maine. The image is centered on Ossipee Lake (43°48′ N, 71°09′ W). Ossipee Mountain is the large circular feature above Ossipee Lake. At the right is the Sandwich Range of the White Mountains. The radar incidence angle is 34°. (c) Volcanic terrain along the southeastern coast of the island of Hawaii. Lava flows, cinder cones, and calderas are clearly visible. At right is the Kilaweia crater. Radar incident angle is 28°.

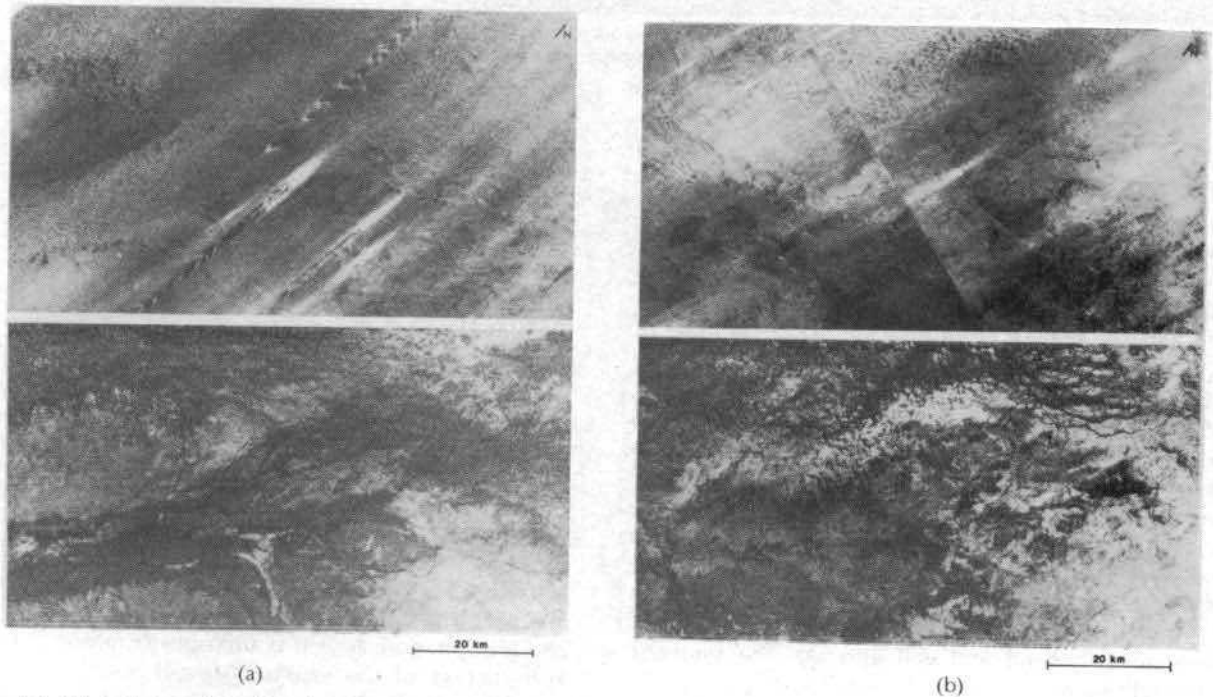

(a) (b)

Fig. 15. (a) SIR-A (bottom) and Landsat (top) images of a 50 × 100 km area of the Egyptian–Sudanese border. The Landsat image shows a landscape dominated by aeolian processes. The Selima sand sheet blankets the underlying material with windblown sand to a few meters thickness. Presently, active dunes marching across the sand sea are visible as the diagonal streaks near the image center. In contrast, the SIR-A image reveals a landscape carved by fluvial processes, now buried beneath the sand. The confluence of what were two large rivers is shown in the center of the SIR-A image. Note that the dunes in the Landsat image have no expression on the SIR-A image. SIR-A image from data take 28, rev 27, acquired November 14, 1981. Landsat band 6 image, November 11, 1972. (b) SIR-A (bottom) and Landsat (top) images of an area in southwestern Egypt. Once again, the Landsat image primarily shows a landscape dominated by aeolian processes, with dunes and the sand sheet forming most of the visible features. The SIR-A image reveals fluvial landforms buried by the sands. Note in particular the braided stream channels near the top of the SIR-A image. The line on the Landsat image is a slight break in the mosaic, the effect of which is heightened by the disparate sun angles. SIR-A image from data take 28, acquired November 14, 1981. Landsat band 6 image November, 1972 (left) and February 9, 1973 (right) (images courtesy of R. Blom, JPL).

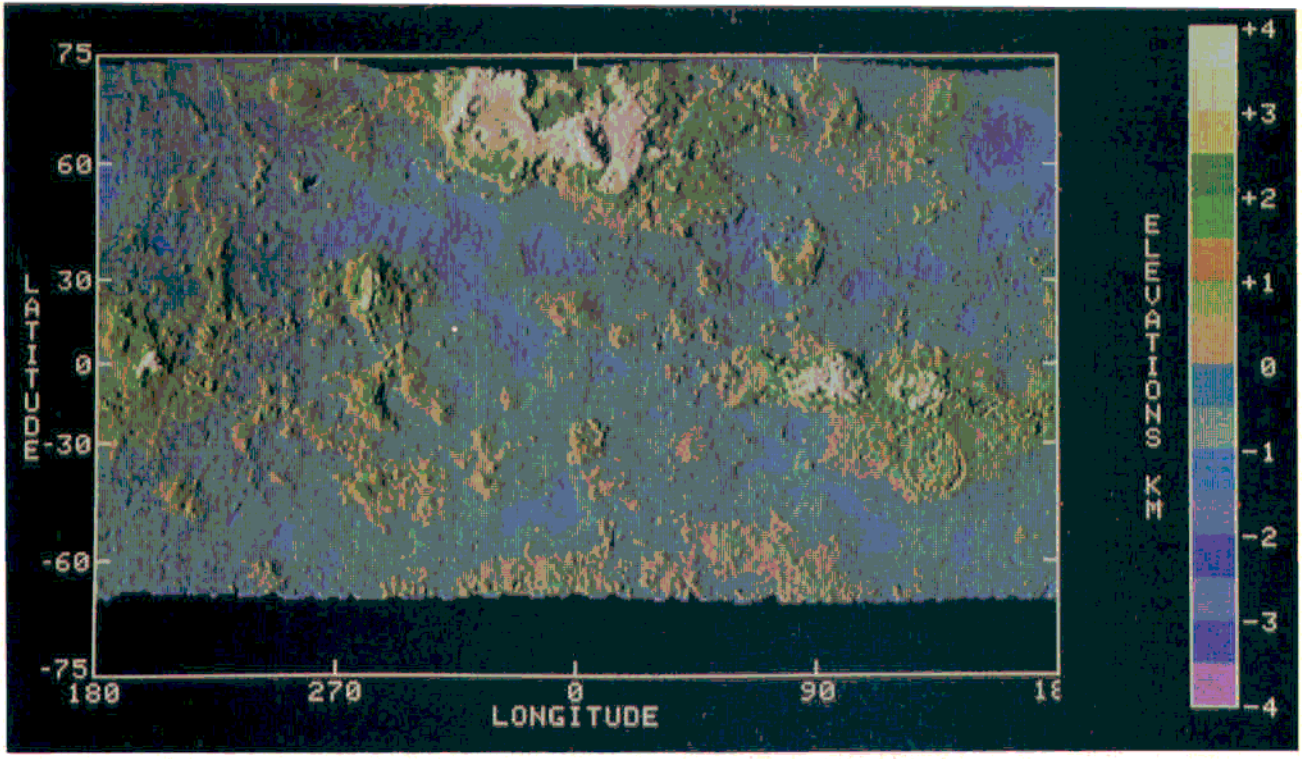

Fig. 14. Global relief map of Venus in Mercator projection. The colors represent constant levels as shown on the right. Shaded relief enhancement has been superimposed to show three-dimensional effect.

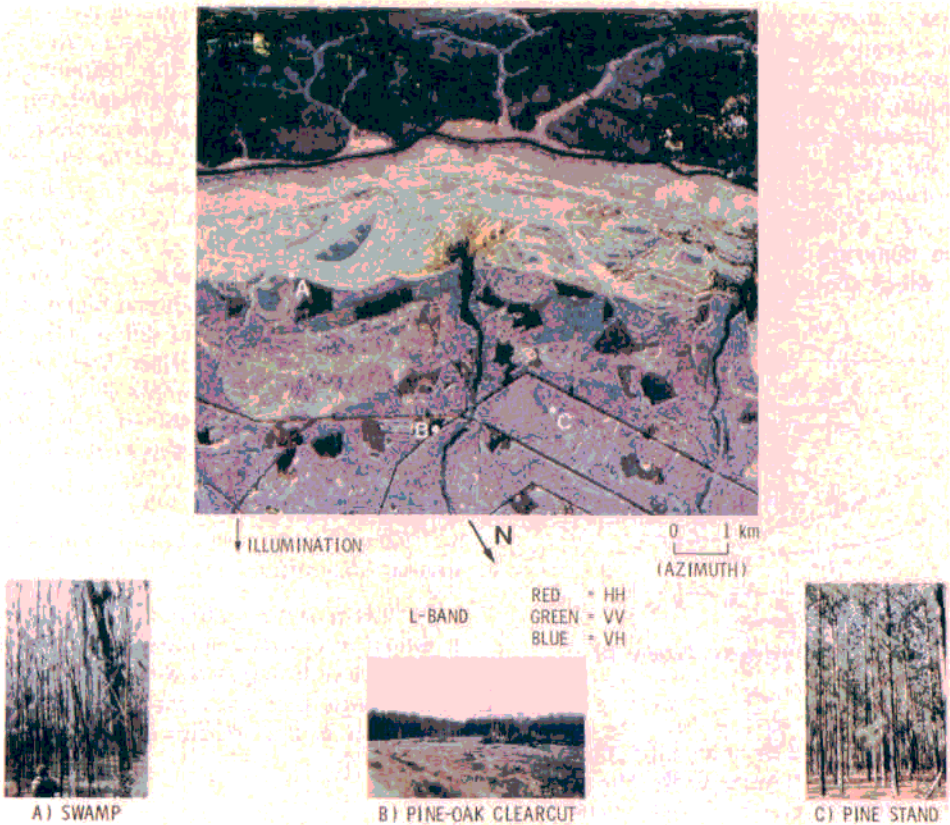

Fig. 13. Multipolarization *L*-band aircraft SAR images of the Savannah River area in South Carolina. Cypress–tupelo association appears pale yellow on the color composite. Distinction of hardwood island (reddish-blue) and marsh on tributary deltas (yellow) in swamp areas is unclear on black and white images. Clearcuts and open water appear dark (image and interpretation courtesy of JPL).

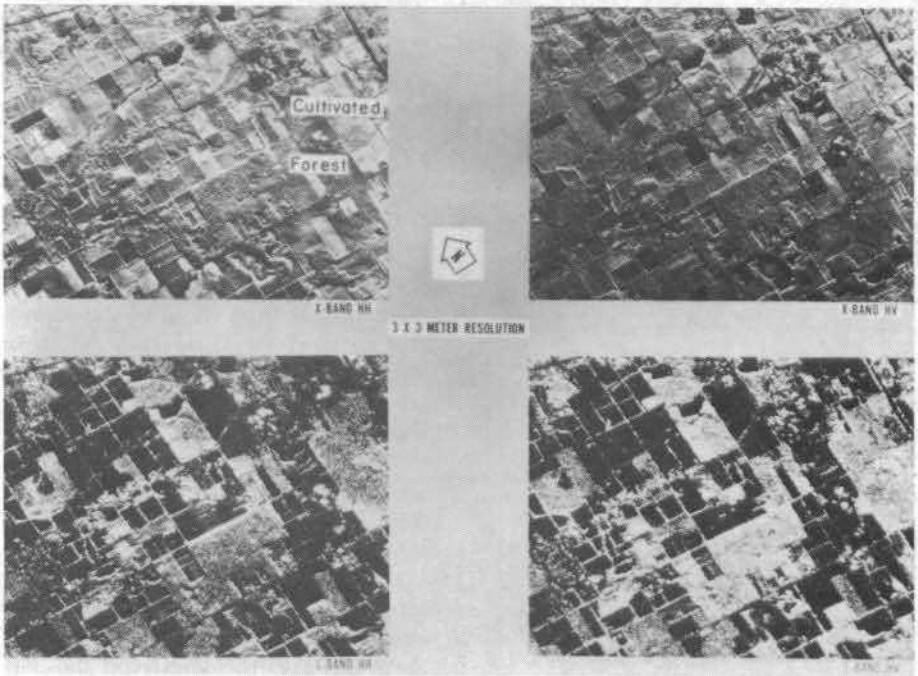

Fig. 12. Dual-frequency dual-polarization images of the Saginaw forest area near Ann Arbor, MI (images courtesy of ERIM).

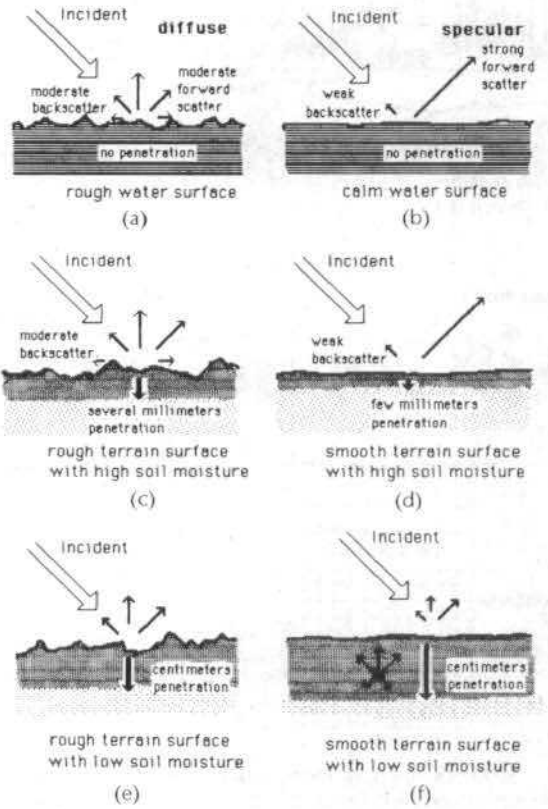

Fig. 8. (a) An incident radar wave on a rough water surface scatters in a diffuse fashion with only weak dependence on scattering angle, and moderate backscatter. (b) When the water surface is calm, the scattering is specular, with most of the energy scattering in the forward and relatively little in the direction back toward the radar. There is virtually no penetration of the water because of its high dielectric constant. (c) An incident wave on rough terrain surface with high soil moisture also scatters diffusely, and a very small penetration of the soil takes place. (d) When the wet soil is relatively flat, there is strong specular scattering away from the radar. (e) and (f) When the soil is dry (e.g., sandy soil in arid regions), there can be penetration ranging from a few centimeters to a few meters, depending on soil aridity.

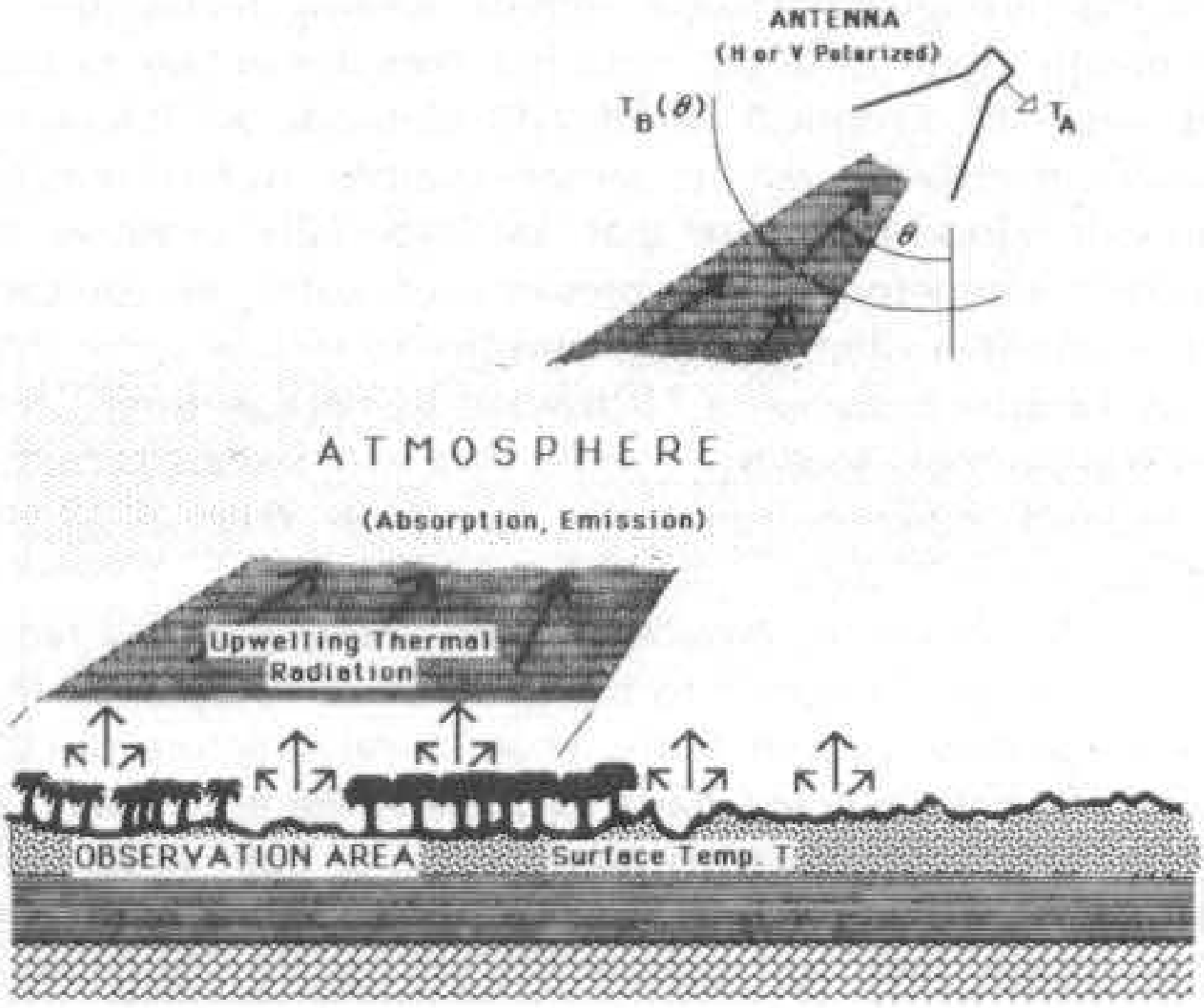

Fig. 3. Illustrating thermal emission process from earth, and radiative transfer of thermal noise energy to a spaceborne radiometer.

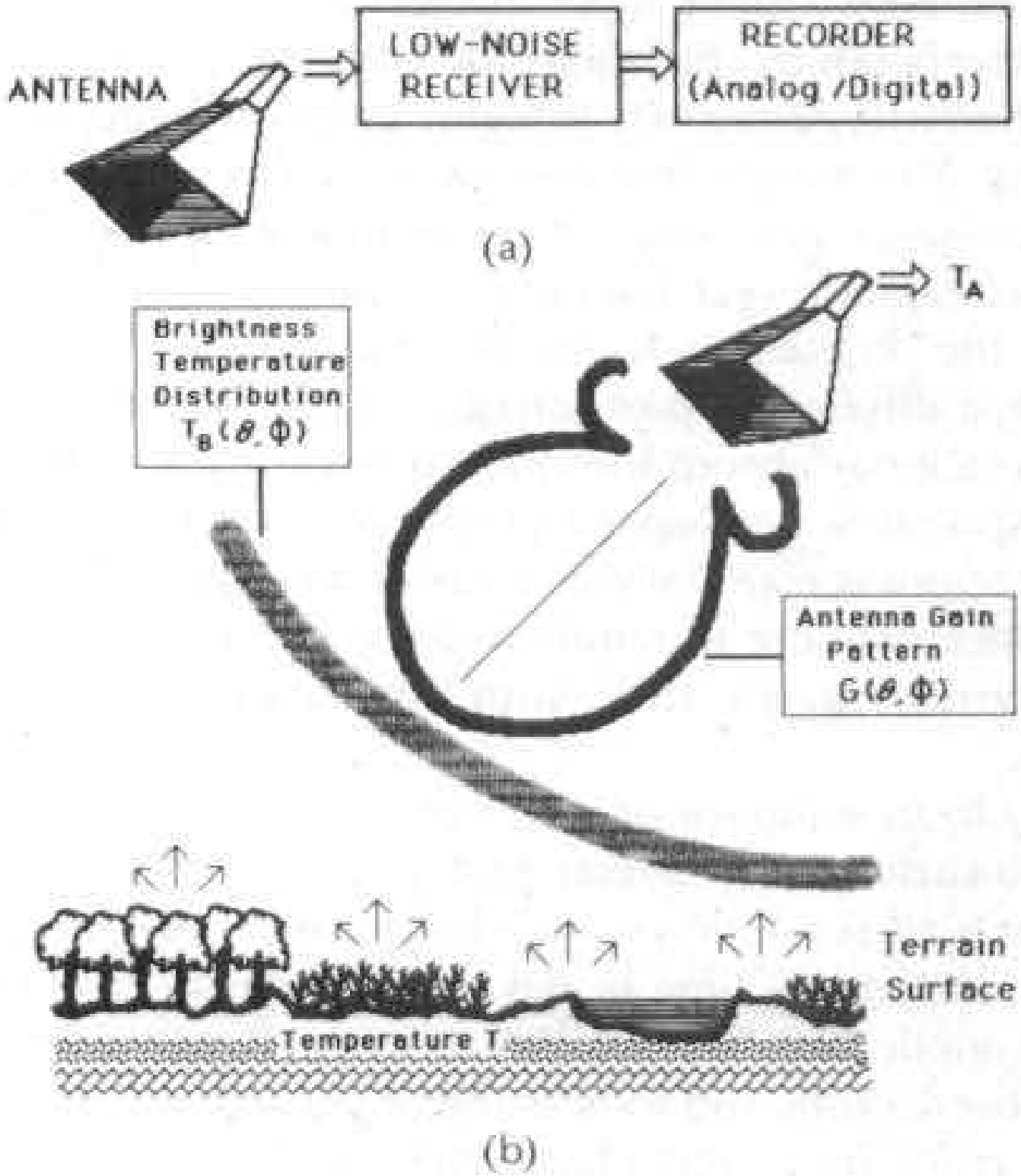

Fig. 2. (a) Simple microwave radiometer showing antenna, receiver, and recording device. (b) A brightness temperature distribution $T_B(\theta, \phi)$ incident on an antenna with a gain pattern $G(\theta, \phi)$.